

A Combined 3D-QSAR, Pharmacophore Modelling, and Molecular Docking Study for Plastoquinone Analogues

Mehmet ÇINAR^{1*}

¹ Bayburt University, Vocational School of Technical Sciences, Electricity and Energy Department, Bayburt, Turkey
cnr.mehmet@gmail.com (ORCID:0000-0002-0184-0082)

Abstract

In this study, a set consisting of 39 compounds that are in the literature and carrying Plastoquinone analogues was investigated. The 3D-QSAR study was performed using a field-based method and Partial Least Square (PLS) regression analysis. The generated 3D-QSAR model has sufficient statistical significance and acceptable prediction power with the regression correlation coefficient (r^2) at 0.97 and $q^2 = 0.4$. The pharmacophore modelling was carried out and a four-point model (AHHR_3) was generated. Molecular docking was performed with the selected IIEP protein and the RMSD value for the position of the ligands docked at the two identified active sites was obtained as 0.3669 Å and 0.5535 Å. Docking analysis revealed that the ABQ16 is the best docked ligand with a DockScore of -9.55, followed by AQ2, AQ6 and ABQ11 with scores of -8.56, -8.2 and -7.64, respectively. It was seen that hydrophobic interactions are dominate and the TYR253 residue is responsible for the pi-pi interaction with the aromatic ring.

Keywords: Plastoquinone Analogues, 3D-QSAR, Pharmacophore Modelling, Molecular Docking, Charge Density

1. Introduction

Cancer is one of the major public health problems that affects people all over the world regardless of sex, age, race or socioeconomic status. According to the World Health Organization (WHO), “Cancer arises from the transformation of normal cells into tumour cells in a multi-stage process that generally progresses from a pre-cancerous lesion to a malignant tumour.” It is the second leading cause of death globally, and causes approximately 10 million deaths per year. It was estimated that more than 1.800.000 cancer cases of different types will be diagnosed in the USA and will cause more than 600.000 deaths in total for the 2020 (Siegel et al., 2016). For this reason, various treatment methods -including surgery- and drugs have been developed to struggle this fatal disease, which has many different types. Chemotherapy is one of the most common treatments used to slowdown the growth of cancer cells or kill cancer cells (Brannon-Peppas & Blanchette, 2004), but chemotherapeutic resistance appears to occur in cancer cells over time, as well as many negative side effects of chemotherapy (Wellington, 2015). Moreover, each cancer type expresses a different drug-resistant gene sequence, and cancerous cells show enormous heterogeneity with respect to drug resistance. The rapid growth of drug-resistant variants because of strong selection imposed by anti-cancer drugs causes many cancers to rapidly acquire drug resistance (Gottesman, 2001). In addition, more than 95% of drugs/compounds that kill cancer cells in culture or regress tumors in studies for animals fail in Phase I studies for humans. Although approved by regulatory agencies such as the FDA, many anticancer drugs have been shown to have no effect on the survival of cancer patients or can provide an increase in overall survival in few months

Received:15.09.2022

Accepted:26.11.2022

Published:15.12.2022

Corresponding author: Mehmet ÇINAR, Bayburt University, Vocational School of Technical Sciences, Electricity and Energy Department, Bayburt, Turkey.

E-mail: cnr.mehmet@gmail.com

Cite this article as: M. Çınar, A Combined 3D-QSAR, Pharmacophore Modelling, and Molecular Docking Study for Plastoquinone Analogues, Eastern Anatolian Journal of Science, Vol. 8, Issue 2, 6-30, 2022.

(Kunnumakkara et al., 2019). Since more than one genes causes many types of cancer, multi-targeted therapies are needed for cancer prevention and treatment, and new anticancer drugs continue to be developed. In addition to advanced clinical trials, products in the drug discovery market are also being improved with new and advanced technologies. Several approaches like reengineering of mesoscale network models to predict the mode of action of tyrosine kinase inhibitors, antibody-drug conjugate-based therapeutic approaches, new virtual screening strategies and methodologies, three-dimensional culture systems for determining anticancer drug effects, integration of computer-aided drug design with network analysis for functional genomic studies have been recently applied in cancer researches to determine the drug-target interactions and discover the new targets (Olgen, 2018). It takes many years for a new drug to be approved by the FDA after in vitro and in vivo research and clinical trials. Due to the complexity of cancer, clinical trials of anticancer drugs take, on average, 1.5 years longer than other drugs (Kunnumakkara et al., 2019). The use of computational methods to complete this process in a shorter time and for appropriate drug design and synthesis has recently received increasing attention. Hence, computational methods play a critical role in drug discovery and are gaining popularity and success because of the ability to develop physical and chemical models by simulating bio molecular processes and discover the robust molecule before it is synthesized.

The quinone moiety is one of the most important structures in drug discovery and found in numerous natural products. Especially aminoquinones are accepted as pharmacological active substances due to their anticancer (Brandy et al., 2012) (Wellington et al., 2019), antibacterial (Jordão et al., 2013) (Janeczko et al., 2016), antifungal (Ryu et al., 2014) (Glamočlija et al., 2018), antiviral (Sendl et al., 1996), antimalarial (Belorgey et al., 2013) and antitubercular (Dey et al., 2014) activities. Thymoquinone (TQ) analogues have been reported to have anti-cancer effects on pancreatic (Banerjee et al., 2010) and ovarian cancer (Johnson-Ajinwo et al., 2018) cell lines. Bayrak et al. synthesized Plastoquinone analogs as a class of anticancer agents and examined their anticancer effects (Bayrak et al., 2020) (Bayrak et al., 2019) (Ciftci et al., 2019).

Therefore, in this study, a set consisting of 39 compounds that are in the literature (Bayrak et al., 2020) (Bayrak et al., 2019) (Ciftci et al., 2019) and carrying Plastoquinone analogues was investigated. Using the experimental activity values of these ligands reported in literature, a Field-based 3D-QSAR study and pharmacophore modeling was performed. Molecular docking study was performed to investigate the interactions with the IIEP protein and the best scores were determined among the investigated ligands. Finally, since charge distribution is an important factor in protein-ligand interactions, the electrical charge properties of some ligands were investigated by different methods.

2. Materials and Methods

Chlorinated plastoquinone (PQ) analogs (Bayrak et al., 2020), aniline containing alkoxy group(s) PQ analogues (Bayrak et al., 2019) and amino-1,4-benzoquinone series (Ciftci et al., 2019) have been synthesized and, biological and anti-cancer activities were reported by Bayrak et al. In these studies, in the literature, a set of 39 ligands were selected by eliminating ligands whose activity values are not significant. For better comparison and linear arrangement, the inhibitory potencies of 39 compounds in the experimental data set, given as molar values (IC_{50}), were converted into pIC_{50} values ($pIC_{50} = 6 - \log_{10} IC_{50}$). The activities of the investigated ligands ranged from 4.64 to 6.04 (pIC_{50}). The compounds were drawn in 2D sketcher module of Maestro program package (Schrödinger Release, 2020) and then converted into 3D. The most important step of the pharmacophore model is to determine the appropriate training set, because this directly determines the quality of the generated pharmacophore. To build the 3D-QSAR model, the data set was divided in the ratio of 80:20. 27 compounds from data set were randomly selected as training set and remaining 12 compounds were used as test set, in considering with structural characteristics and biological activities. The energy minimization of compounds was performed by LigPrep (Schrödinger Release: LigPrep, 2020) module of Maestro software. The 3D-QSAR model was build using the Partial Least Square (PLS) regression analysis, the grid spacing was kept at 1 Å and 5 PLS factors were included in the model development. PHASE (Pharmacophore alignment and

scoring engine) (Schrödinger Release: Phase, 2020) which is an effective instrument for the superposition of flexible ligands (Miller et al., 1999), was used to create pharmacophore and 3D-QSAR models. The spatial arrangements of functional groups that are typical and necessary for the biological activity of the ligands used in the study can be defined by PHASE (Evans et al., 2007). Ligands with experimental pIC₅₀ values greater than 5.6 were designated as actives and < 4.8 as inactives, and the remaining compounds not meeting these breakpoints were considered moderately active. To generate the three-dimensional coordinates for all ligands, LigPrep was used (Schrödinger Release: LigPrep, 2020). The Epik (Greenwood et al., 2010) (Shelley et al., 2007) (Schrödinger Release: Epik, 2020), which is based on the more accurate Hammett and Taft methodologies was applied to generate the ionization/tautomeric states. The IIEP protein was obtained from Protein Data Bank (Bernstein et al., 1977) (Berman et al., 2000). The Protein Preparation Wizard (PrepWizard) in Maestro was used to prepare the protein IIEP following the steps outlined in Ref (Madhavi Sastry et al., 2013) but OPLS3e (Harder et al., 2016) was used as the force field. The docking analysis was done basing on creation of a receptor grid using the extra precision (XP) docking protocol in Glide (Schrödinger Release: Glide, 2020), after the protein preparation and specify the active binding sites of protein.

To elucidate the interactions between crystal molecules, Hirshfeld surface analysis was performed using the available *.cif files of the crystals by Crystal Explorer 3.1 program package (Turner et al., 2017). To identify the the intermolecular interactions and electric charge characteristics of studied molecules, Molecular Electrostatic Potential (MESP), Frontier Molecular Orbital (FMO) and Mulliken Charge Analysis was performed. In order to carry out the aforementioned analyzes, first of all, it is necessary to determine the optimum geometry of each molecule at the minimum energy level. Density functional theoretical (DFT) calculations were performed at the B3LYP (Becke's three parameter Lee–Yang–Parr) (Lee et al., 1988) (Becke, 1988) /6-31G(d,p) level of theory and using the Gaussian 09 program package (Frisch et al., 2016) to obtain optimized geometries of each PQ molecule.

3. Results and Discussion

3.1 Field-Based 3D-QSAR and Pharmacophore Modeling

QSAR modeling is an effective tool as it explores and uses the relationship between chemical structure and biological action in the development of new drug candidates (Tropsha, 2010). The Field-Based QSAR is a tool similar to CoMFA/CoMSIA, used to create a model for the relationship between 3D properties of a number of aligned compounds and known activity values. However, the models are not actually equivalent to standard CoMFA and CoMSIA models and often-different names are used, such as Force Field for CoMFA-like models and Gaussian Field for CoMSIA-like models. The Force Field consists of a steric field based on the Lennard-Jones potential and an electrostatic field with a dielectric dependent on a $1/r^2$ dependent distance, while the Gaussian based potential consists of five fields, namely steric, electrostatic, hydrophobic, hydrogen bond acceptor (HBA) and hydrogen bond donor (HBD). In this study, Gaussian field-based was preferred to create the 3D-QSAR model.

The dataset was divided into two parts to form the randomly selected 27 compounds as training sets and the remaining 12 compounds as test sets. The structural properties of the compounds in these sets, the experimentally recorded biological activity values (both IC₅₀ and pIC₅₀), the predicted activities generated by the created model and the predicted error between recorded and estimated activity values are given in Table 1. The conformers obtained by energy minimization were used in the alignment of molecules, as shown in Fig. 1. The 3D-QSAR model was constructed using Partial Least Square (PLS) regression analysis, keeping the grid spacing at 1 Å and including 5 PLS factors in the model development. PLS offers the below statistical measures; standard deviation of regression (SD) which is the root mean square (RMS) error in the fitted activity values, regression correlation coefficient (R²) that indicates the variance in observed activities, R² scramble, stability, ratio of the model variance to the observed activity variance (Fisher test or F test or variance ratio), significance level of variance ratio (P value), root mean square error of test

set (RMSE), cross-validated correlation coefficient for the test set (Q^2) by leave one out (LOO) method and Pearson-r values. The best alignment-dependent and Gaussian field-based model was achieved with PLS factor 5. While the experimental and predicted biological activity values with PLS factor 5 are given in Table 1, Table 2 shows a summary of the statistical results obtained for this model. For the specified model, it can be seen in Fig. 2 that there is a linear correlation between the actual and predicted activity values of the training set compounds. As seen in Table 2, the percentage contribution of steric, electrostatic, hydrophobic and hydrogen bond donor (HBD) were 0.423, 0.074, 0.375 and 0.128, respectively whereas the no contribution was obtained for the hydrogen bond acceptor (HBA). The contour plot analysis of studied compounds is given in Fig. 3. The most remarkable contribution was found due to steric effect for the Plastoquinone analogs activity, followed by hydrophobic which means that for protein-ligand interactions, this means that the steric field is more important than the electrostatic groups. The green color represents the favorable steric field region in the steric contour map, and the unfavorable steric field region is usually shown in a different color, however, Fig. 3 (a) indicates that no such region was detected and a bulky-group may be added to the green-colored zone for a larger activity value. The distribution of positive and negative electrostatic regions is characterized by electrostatic contour map. Negative charges are displayed by red and positives by blue. Similarly, in the hydrophobic counter map, the colors show us the regions where these molecules are suitable (yellow) and unsuitable (white) for hydrophobic or lipophilic groups for better activity. Positive (dark red) and negative (purple) regions indicate that the activity will increase and decrease in the presence of HBD groups, respectively, in HBD contours. A quick look at the statistics of the model created for 3D-QSAR, it is seen that the R^2 value is 0.97 and the stability value is calculated as 0.82. While a value of 0.4 was found for Q^2 , SD was obtained at 0.08, Pearson-r at 0.85 and R^2 CV that derived from the LOO cross-validation method at 0.75. Godoy-Castillo et al. (Godoy-Castillo et al., 2021) studied the potent inhibitory effect of 33 naphthoquinone derivatives on heat shock 90 protein using a method similar to that in this study. In the QSAR modeling, the variance was calculated as 97%,

the standard deviation was found to be 0.06, and the Q^2 was obtained as 0.71. Based on these statistical data, it was stated that the model resulted in sufficient statistical significance and acceptable predictive power. Acuna et al. (Acuña et al., 2018) reported statistical parameters of CoMFA model for 18 quinone derivatives as $r^2 = 0.99$ and $q^2 = 0.625$. In a study performed for 52 heterocyclic quinones (Shi et al., 2021) with three different 3D-QSAR models, r^2 was calculated as 0.93, 0.94 and 0.95 and q^2 was calculated as 0.75, 0.59 and 0.73 for each model. In this study, ligands with recorded pIC_{50} values greater than 5.6 were determined as actives and those with < 4.8 as inactive, to generate pharmacophore and 3D-QSAR models, while the remaining compounds that did not meet these breakpoints were considered moderately active. A set of three pharmacophore features was built by PHASE: two hydrophobic (H), a hydrogen bond acceptor (A) and an aromatic ring (R). To test the reliability of the models, the enrichment report was also generated basing on the hypo score, enrichment factor (EF), ROC (Receiver operating characteristics area under the curve), BEDROC (Boltzmann-enhanced Discrimination Receiver Operator Characteristic area under the curve), AUAC (Area under the accumulation curve) and matches for the AHHR_3 which selected as the best pharmacophore model due to the highest scores, as shown in Table 3. While the distances and angles between the different regions of this model are given in Fig. 4, Fig. 5 displays the mapping of all chemical properties of this differential pattern on active and inactive compounds.

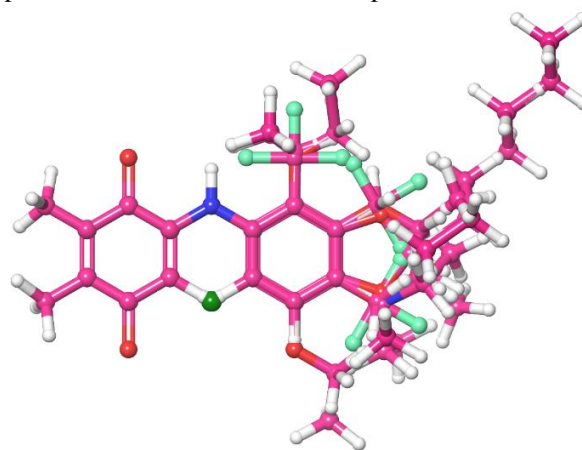


Figure 1. The alignment of 39 ligands used in dataset

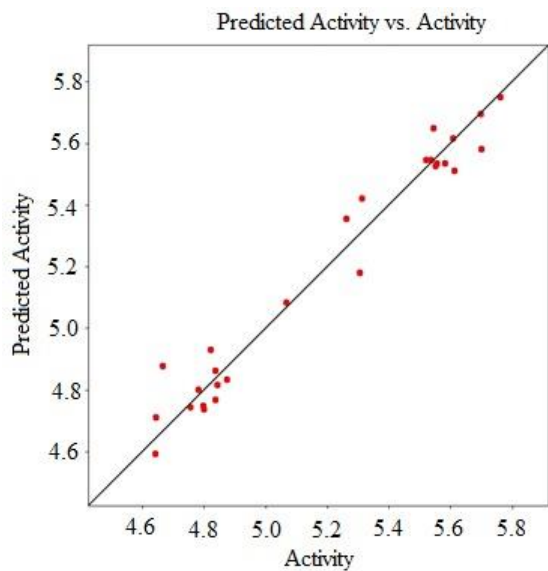


Figure 2. Scattered plots of experimental and predicted activity values for training set

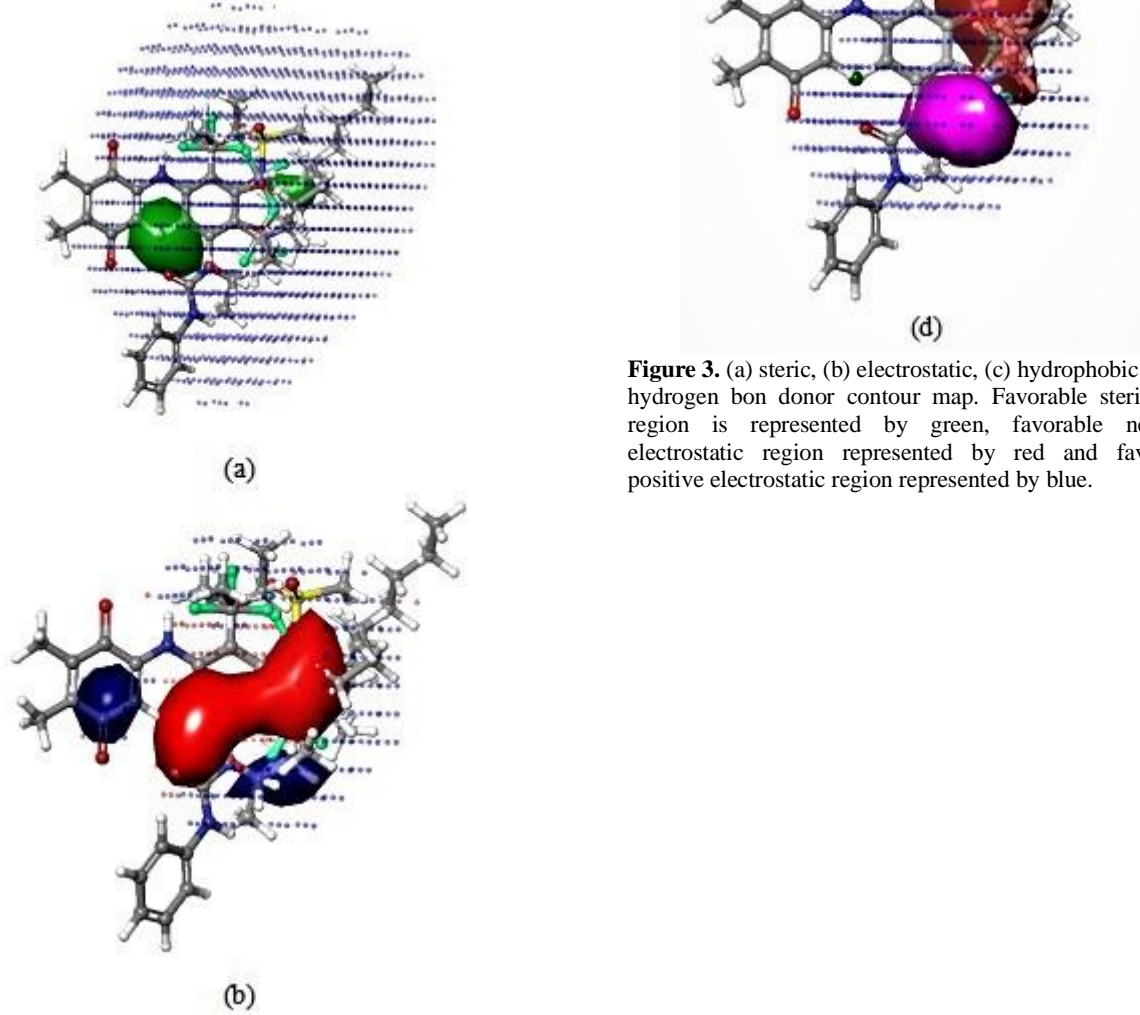


Figure 3. (a) steric, (b) electrostatic, (c) hydrophobic and (d) hydrogen bond donor contour map. Favorable steric field region is represented by green, favorable negative electrostatic region represented by red and favorable positive electrostatic region represented by blue.

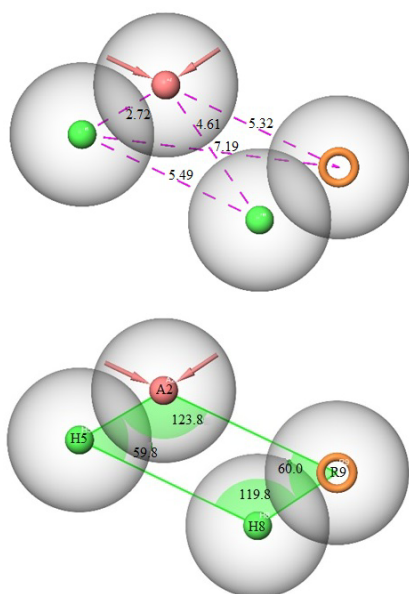


Figure 4. 3D-pharmacophore model with its corresponding chemical features for AHHR_3. (a) Intersite distances between the pharmacophoric points, (b) Intersite angles between the pharmacophoric points (A: Acceptor; H: Hydrophobic; R: Aromatic ring)

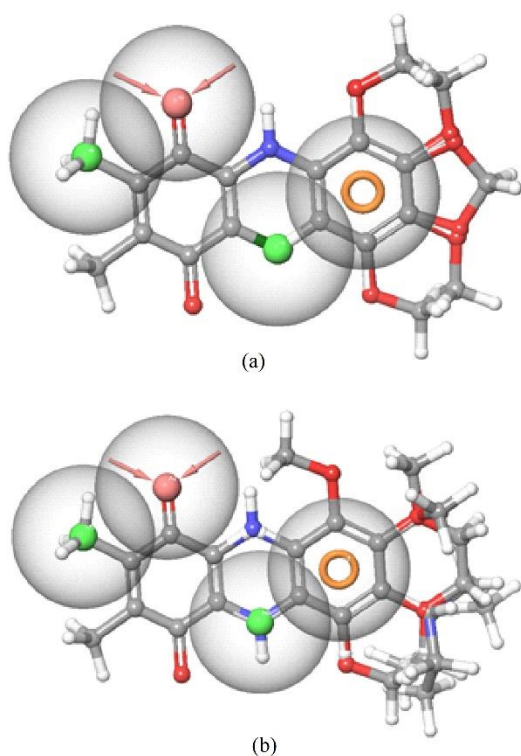


Figure 5. Mapping of the chemical features for active (a) and inactive (b) compounds onto the AHHR_3 pharmacophore model

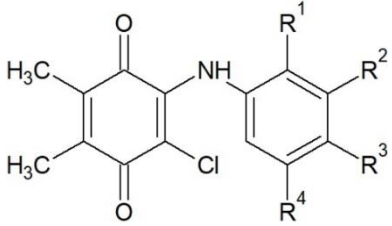
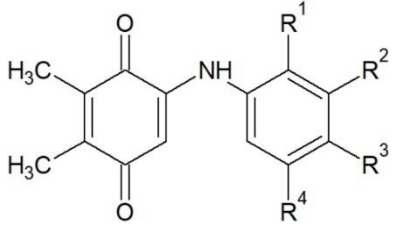
3.2 Ligand and Protein Preparation

It is well known that to exploit the structure of protein-ligand or protein-protein binding sites is aimed in structure-based drug design. In addition, it is extremely important to know which binders or docking hits are complementary to the receptor in lead optimization. Hence, the prepared protein structure of IIEP was uploaded into SiteMap, which generates various physicochemical properties (*Schrödinger Release: SiteMap*, 2020) (T. Halgren, 2007) (T. A. Halgren, 2009) and top five possible binding sites and determined their potential druggability were obtained. If the SiteScore value produced by software is 1.0 and above, it indicates a high druggability and this is used as a measure to define hydrophobicity, along with another value produced, DScore (Vidler et al., 2012). The generated scores for those sites are presented in Table 4. Although SiteScores obtained for sitemap, 4 and 5 are lesser than one, the difference is not much, and that means all binding pockets are having capability to bind different types of ligands. In this case, no binding pocket should be ignored, hence, all five sites (see Fig. 6) were handled for analysis. The region generated as sitemap 1 and 2 are accommodate the co-crystallized ligands for protein IIEP (Nagar et al., 2002).

3.3 Molecular Docking

One of the most widely used computational tools for the prediction of binding modes in protein-ligand interactions is molecular docking (Sousa et al., 2013). An accurate and comprehensive understanding of molecular interaction/recognition and knowledge of structural data as well as molecular protein-ligand binding mechanisms are of great importance for drug design, development, and discovery (Du et al., 2016). Docking analysis was performed after preparation of the protein and identification of active binding sites of the protein, as mentioned above. Docking analysis was performed by applying the extra precision (XP) docking protocol to the creation of a receiver grid. The co-crystallized ligands are also included for comparison of experimental and docked pose of the ligand, and given in Fig. 7. The RMSD values were obtained as 0.3669 Å, 0.5535 Å for sitemap 1 and 2, respectively. RMSD values up to 2 Å are accepted for

Table 1. The evaluated data set with their activity, classification and predicted activity by the Field-based 3D-QSAR model.

													
	R ¹	R ²	R ³	R ⁴	IC ₅₀ , μM	pIC ₅₀	Predicted activity*	Predicted error	Dataset				
ABQ1	OCH ₃	H	H	H	2.78	5.56	5.56	0.00	training				
ABQ2	H	OCH ₃	H	H	2.01	5.70	5.63	-0.06	training				
ABQ3	H	H	OCH ₃	H	1.51	5.82	5.45	-0.37	test				
ABQ4	OCH ₂ CH ₃	H	H	H	2.81	5.55	5.57	0.02	training				
ABQ5	H	OCH ₂ CH ₃	H	H	2.84	5.55	5.66	0.12	test				
ABQ6	H	H	OCH ₂ CH ₃	H	2.01	5.70	5.35	-0.35	test				
ABQ7	H	H	O(CH ₂) ₃ CH ₃	H	2.44	5.61	5.57	-0.05	training				
ABQ8	H	H	O(CH ₂) ₅ CH ₃	H	4.95	5.31	5.35	0.05	training				
ABQ9	H	H	O(CH ₂) ₇ CH ₃	H	5.47	5.26	5.33	0.07	test				
ABQ10	OCH ₃	H	OCH ₃	H	4.86	5.31	5.49	0.17	training				
ABQ11	OCH ₃	H	H	OCH ₃	0.92	6.04	5.53	-0.50	test				
ABQ12	H	OCH ₃	OCH ₃	H	1.99	5.70	5.56	-0.14	training				
ABQ13	H	OCH ₃	H	OCH ₃	2.85	5.55	5.61	0.07	training				
ABQ14	OCH ₂ CH ₃	H	H	OCH ₂ CH ₃	3.00	5.52	5.55	0.02	test				
ABQ15	H	OCH ₂ O	H	H	1.73	5.76	5.73	-0.03	training				
ABQ16	H	O CH ₂ CH ₂ O	H	H	2.60	5.59	5.58	-0.01	test				
ABQ17	H	OCH ₃	OCH ₃	OCH ₃	2.62	5.58	5.54	-0.04	training				
AQ1	H	H	H	H	13.38	4.87	4.78	-0.09	training				
AQ2	CF ₃	H	H	H	15.89	4.80	4.72	-0.08	training				
AQ6	H	H	CH ₃	H	16.55	4.78	4.74	-0.04	training				
AQ7	CH(CH ₃) ₂	H	H	H	15.59	4.81	4.37	-0.44	test				
AQ9	H	H	N(CH ₂ CH ₃) ₂	H	17.53	4.76	4.78	0.02	training				
AQ11	H	H	H	H	3.01	5.52	5.52	0.00	training				
AQ12	H	CF ₃	H	H	2.92	5.53	5.54	0.00	training				
AQ13	H	H	CF ₃	H	5.48	5.26	5.29	0.02	training				
AQ14	H	CH ₃	H	H	2.29	5.64	5.56	-0.08	test				
AQ15	H	H	CH ₃	H	2.34	5.63	5.49	-0.14	test				
AQ16	CH(CH ₃) ₂	H	H	H	8.58	5.07	5.11	0.04	training				
AQ17	H	H	CH(CH ₃) ₂	H	2.46	5.61	5.60	-0.01	Training				
PQ2	H	OCH ₃	H	H	7.72	5.11	4.89	-0.22	test				
PQ3	H	H	OCH ₃	H	22.75	4.64	4.71	0.06	training				
PQ5	H	OCH ₂ CH ₃	H	H	8.95	5.05	4.92	-0.13	test				
PQ6	H	H	OCH ₂ CH ₃	H	22.79	4.64	4.61	-0.03	training				
PQ9	OCH ₃	H	H	OCH ₃	14.57	4.84	4.79	-0.05	training				
PQ10	H	OCH ₃	OCH ₃	H	14.57	4.84	4.82	-0.02	training				
PQ11	H	OCH ₃	H	OCH ₃	15.07	4.82	4.87	0.04	training				
PQ12	OCH ₂ CH ₃	H	H	OCH ₂ CH ₃	15.95	4.80	4.80	0.00	training				
PQ14	H	OCH ₂ CH ₂ CH ₃	H	21.65	4.66	4.84	0.17	training					
PQ15	H	OCH ₃	OCH ₃	OCH ₃	14.39	4.84	4.80	-0.05	Training				

* Predicted activity for PLS factor 5

Table 2. The statistical values obtained by PLS factor 5.

SD	R ²	R ² CV	R ² Scramble	Stability	F	P	RMSE	Q ²	Pearson-r
0.0772	0.9699	0.7516	0.5976	0.824	135.4	3.07.10 ⁻¹⁵	0.26	0.3993	0.8456
Steric		Electrostatic		Hydrophobic		H-bond Acceptor		H-bond Donor	
0.423		0.074		0.375		0.128		0	

Table 3. Enrichment report for the pharmacophore model which has the highest score (AHHR_3)

Hypothesis	Phase Hypo Score	EF	BEDROC	ROC	AUAC	Total Actives	Ranked Actives	Matches
AHHR_3	1.29	60.3	0.69	0.6	0.76	5	3	4 of 4

EF: enrichment factor, ROC: Receiver operating characteristics area under the curve, BEDROC: Boltzmann-enhanced Discrimination Receiver Operator Characteristic area under the curve, AUAC: Area under the accumulation curve

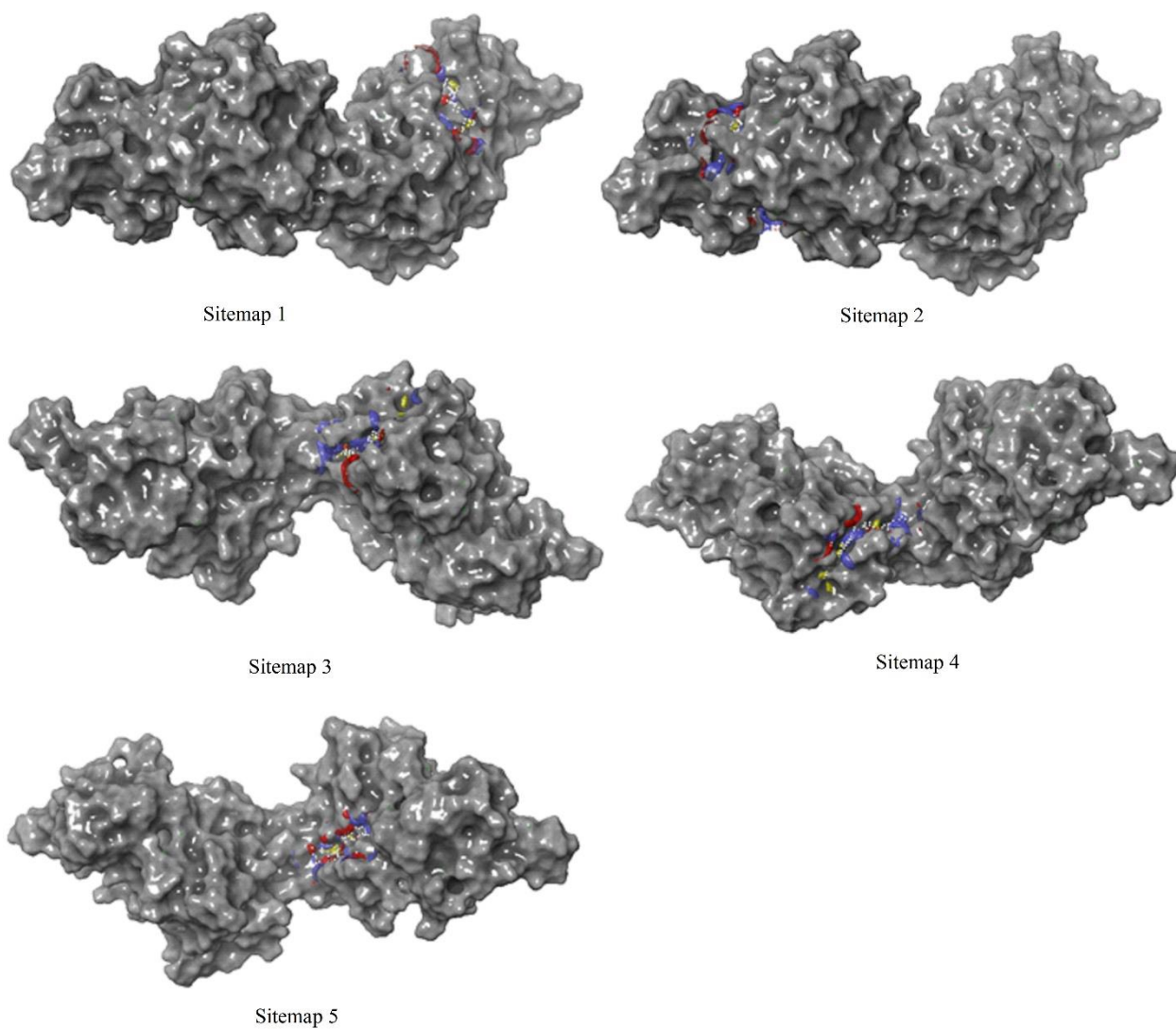
**Figure 6.** Top five possible binding sites of protein 1IEP

Table 4. Sitemap scoring analysis

	SiteScore	size	Dscore	volume
sitemap_1	1.093	327	1.113	848.925
sitemap_2	1.083	299	1.107	733.677
sitemap_3	1.034	100	1.073	197.568
sitemap_4	0.975	91	1.014	198.254
sitemap_5	0.891	70	0.819	203.056

molecular docking procedure, and in this study, low values were obtained for sitemap 1 and sitemap 2, which shows that the applied procedure is valid. Since the docking protocol is able to predict the binding for the crystal ligand correctly, the prediction for the rest of ligands will be also correct. The scores obtained from XP calculations for the sitemap-1 are presented in Table 5. DocScore (or GScore) refers to how good the interaction between drug and protein is, as the stability of docking between ligand and protein depends on the binding interaction. Docking scores are calculated as negative, and higher negative values of DocScore indicates the better binding affinity/interaction with the target protein/receptor (Bassyouni, 2017). As can be seen from table, docking score of the co-crystallized ligand was found to be -15.46, and the ABQ16 has the highest docking score with -9.55 among the studied ligands. Therefore, the interaction between IIEP protein and this ligand are depicted in Fig. 8. 2D interaction diagram of ABQ16 ligand and protein is shown in Fig. 9 with comparison of co-crystallized ligand – protein interaction. Here, the co-crystalline ligand is located in the center and surrounds the residuals almost elliptical. Residuals in more inner elliptical orbits indicate direct contact, while those further out indicate indirect contact. In addition, the size of these elliptical orbits indicates the number of atomic contacts. In the inner orbit, we could find that the residue of TYR253 is important and has a pi-pi interaction with the aromatic ring (Fig. 9(b)). According to the docking studies analysis, hydrophobicity dominates the interactions, and the hydrophobic residues for ABQ16 ligand can be seen in Fig. 10. The hydrogen bond interaction is considered a vital parameter for the stability of the drug-protein complex and was calculated for all molecules with the best score in this study. For instance, the docking score of the AQ2, AQ6, ABQ11 and ABQ9 were obtained as 8.56, 8.2, 7.64 and 7.5, respectively with negative values. In addition, the

hydrogen bond values accompanying them were found to be 0.75, 1.26, 0.73 and 0.35, respectively as shown in Table 5. The results of the present study depicted that the studied Plastoquinone analogues showed good interactions with the IIEP protein.

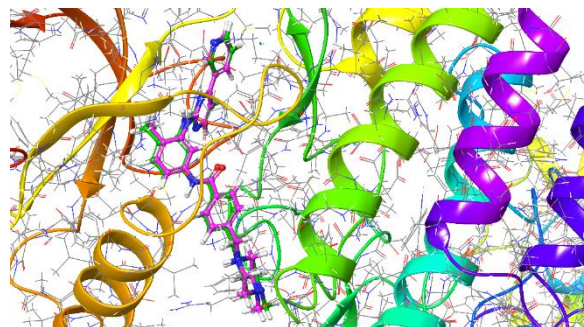


Figure 7. The comparison pose of experimental (magenta) and docked (green) co-crystallized ligand –for sitemap 1

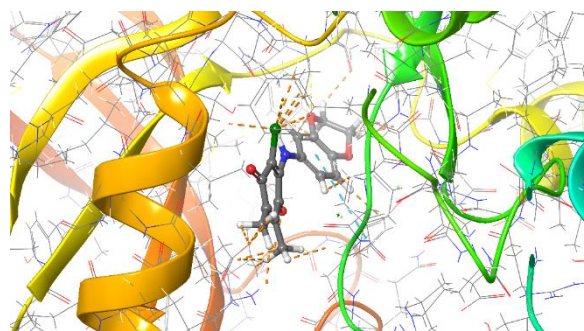


Figure 8. Interaction established between the IIEP protein and ABQ16 ligand obtained through the docking protocol and for sitemap 1 (Hydrogen bonds were depicted as dashed lines in orange and blue dashed lines depict the pi-pi stacking).

A series of 1,4-naphthoquinone derivatives was synthesized and molecular docking was performed *in silico*. Among the 14 synthesized compounds, the highest docking score was obtained as -7.73, and hydrophobic interaction with LYS179 and TRP58 was reported (Ravichandiran et al., 2014). In the computational study to determine the interaction mechanism of the mono and dialkyloxy derivatives of 5,8-quinolinedione with the NQO1 enzyme, it was determined that the 5,8-quinolinedione moiety was bound to the enzyme via hydrophobic interactions and by aromatic residues Trp 105, Tyr 128 and Phe 178 (Kadela-Tomanek et al., 2017). In the study performed by placing 52 heterocyclic quinone

inhibitors in the active site of the NQO1 enzyme, it was determined that most compounds showed π stacking interactions with Trp105, Phe106 and Phe178 (López-Lira et al., 2018).

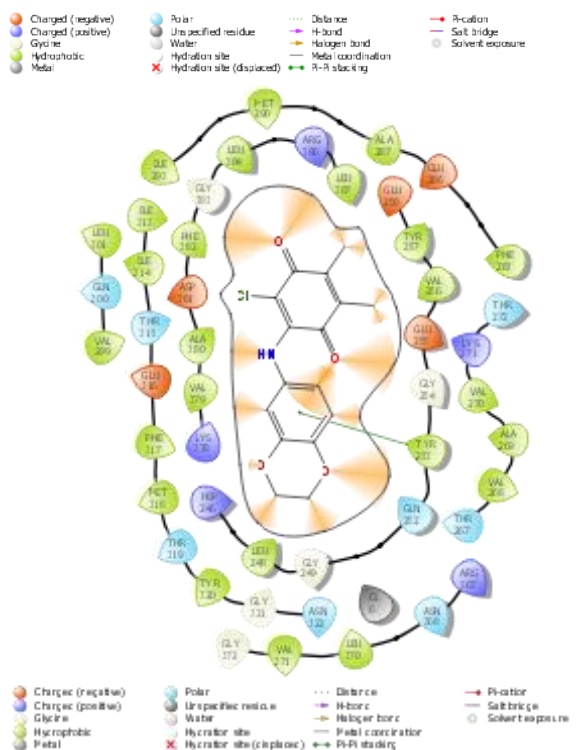
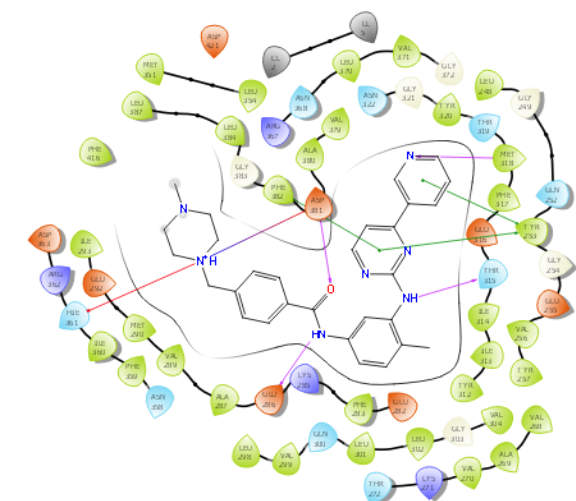


Figure 9. 2D co-crystallized ligand – protein (top), and ABQ16 ligand – protein (bottom) interaction diagram

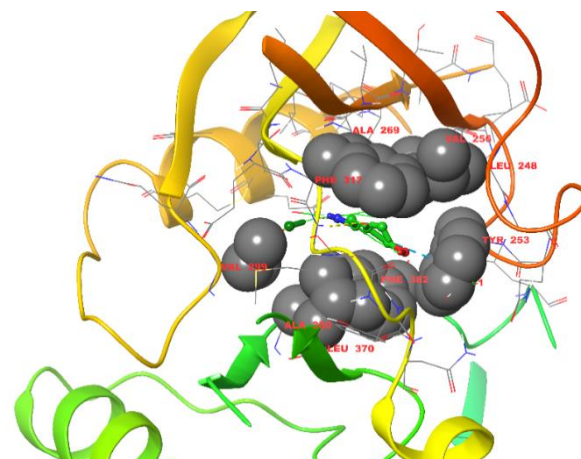


Figure 10. Hydrophobic residues

3. 4 Hirshfeld Surface and MESP Analysis

It is well known that the strength of the interaction between an inhibitor molecule and the specific target identified depends on the chemical characteristics -specifically charge properties- as well as the unique structure of the molecule. Hence, to determine the important interactions Hirshfeld surface and molecular electrostatic potential analysis were done and evaluated. The Hirshfeld surface is defined as the area occupied by a molecule in a crystal by partitioning the crystal electron density into molecular fragments (Spackman & Jayatilaka, 2009) (Spackman & Byrom, 1997). The Hirshfeld surface for a molecule is obtained by scanning van der Waals distances and defining interaction sites (Hirshfeld, 1977). When the Hirshfeld surface is obtained, the parameters d_e , which expresses the distance from Hirshfeld's surface to the nearest nucleus outside the surface, and d_i , which expresses the distance corresponding to the nearest nucleus on the surface, are defined. The normalized contact distance (d_{norm}), which enables the identification of regions of particular importance for intermolecular interactions, is defined as follows, depending on the d_e , d_i , and vdw radii of the atom (Spackman & McKinnon, 2002).

$$d_{norm} = \frac{d_i - r_i^{vdw}}{r_i^{vdw}} + \frac{d_e - r_e^{vdw}}{r_e^{vdw}}$$

Table 5. Docking scores obtained by XP visualizer for sitemap-1

Ligand	GScore	DockScore	LipophilicEvdW	PhobEn	PhobEnHB	PhobEnPairHB	HBond	Electro	Sitemap	PiCat	LowMW	Penalties	HBPenal	ExposPenal	RotPenal
IIEP-ligand1	-15.46	-15.46	-7.17	-2.53	-1.5	0	-1.84	-0.89	-0.33	0	0	0.03	0	0	0.29
IIEP-ligand2	-15.46	-15.46	-7.17	-2.53	-1.5	0	-1.84	-0.89	-0.33	0	0	0.03	0	0	0.29
ABQ16	-9.55	-9.55	-4.63	-2.25	-1	0	-0.53	-0.26	-0.61	0	-0.43	0	0	0	0.16
AQ2	-8.56	-8.56	-4.07	-1.74	0	0	-0.75	-0.57	-1.1	0	-0.5	0	0	0	0.18
AQ6	-8.2	-8.2	-3.47	-1.84	-1	0	-1.26	-0.44	-0.8	0	-0.5	0.86	0	0	0.26
ABQ11	-7.64	-7.64	-4.28	-1	0	0	-0.73	-0.65	-0.71	0	-0.43	0	0	0	0.15
ABQ9	-7.5	-7.5	-5.59	-1.6	0	0	-0.35	-0.03	-0.35	0	-0.2	0.12	0	0	0.49
AQ1	-7.44	-7.44	-4.35	-1.66	0	0	-0.36	-0.12	-0.73	0	-0.5	0	0	0	0.28
ABQ8	-7.14	-7.14	-5.27	-1.32	0	0	-0.35	-0.01	-0.33	0	-0.29	0	0	0	0.44
AQ7	-6.67	-6.67	-4.67	-1.19	0	0	-0.7	-0.13	-0.68	0	-0.5	1	0	0	0.21
ABQ5	-6.2	-6.2	-4.6	-1.37	0	0	-1.33	-0.37	-0.66	0	-0.48	2.35	0	0	0.25
ABQ10	-6.19	-6.19	-4.95	-0.45	0	0	-0.7	-0.1	-0.72	0	-0.43	1	0	0	0.15
ABQ14	-6.1	-6.1	-5.11	-0.45	0	0	-0.65	-0.13	-0.7	0	-0.33	1	0	0	0.27
ABQ7	-5.87	-5.87	-4.19	-0.85	0	0	-0.35	-0.07	-0.41	0	-0.39	0.02	0	0	0.36
ABQ6	-5.76	-5.76	-4.8	0	0	0	0	-0.12	-0.62	0	-0.48	0	0	0	0.25
ABQ12	-5.6	-5.6	-3.56	-0.62	0	0	-0.59	-0.28	-0.27	0	-0.43	0	0	0	0.15
ABQ15	-5.6	-5.6	-4.23	-0.86	0	0	-1.33	-0.16	-0.65	0	-0.48	1.95	0	0	0.17
AQ9	-5.5	-5.5	-4.36	0	0	0	-0.32	-0.16	-0.52	0	-0.5	0.1	0	0	0.26
ABQ17	-5.43	-5.43	-3.48	-0.57	0	0	-0.57	-0.46	-0.33	0	-0.33	0	0	0.18	0.13
ABQ13	-3.33	-3.33	-2.41	-0.12	0	0	-0.51	-0.09	-0.21	0	-0.43	0.01	0	0.27	0.15

GScore & DockScore: Docking Score; LipophilicEvdW: ChemScore lipophilic pair term and fraction of the total protein-ligand van der Waals energy; PhobEn: hydrophobic enclosure reward; PhobEnHB: reward for hydrophobically packed H-bond; PhobEnPairHB: reward for hydrophobically packed correlated H-bond; HBond: ChemScore H-bond pair term; Electro: electrostatics reward; Sitemap: sitemap ligand/receptor non H-bonding polar/hydrophobic and hydrophobic/hydrophilic complementarity terms; PiCat: reward for pi-cation interaction; LowMW: reward for ligands with low molecular weight; Penalties: polar atom burial and desolvation penalties, and penalty for intra-ligand contacts; HBPenal: penalty for ligands with large hydrophobic contacts and low H-bond scores; ExposPenal: Penalty for exposed hydrophobic ligand group; RotPenal: Rotatable bond penalty.

The 3D Hirshfeld surfaces of ABQ10, ABQ14, ABQ17, AQ9, AQ11, AQ17, PQ11 and PQ14 were obtained and illustrated in Fig. 6 showing surfaces that have been mapped over d_{norm} . Here, the red dots show the stronger hydrogen bonds. The d_{norm} region for each molecule is given in the Armstrong (\AA) unit below the corresponding surface in Table 6. The O-H interactions can be seen in the Hirshfeld surface as bright red dots and the C-H \cdots O interactions in light red spots, here as the H \cdots H contacts are represented with the other visible spots on the surface. To highlight the close contacts of certain pairs of atoms, for example H-H, O-H/H-O and C-H/H-C, a 2D fingerprint plot of the surfaces is presented in Table 7 comprising the partial contribution of the whole surface. When one molecule is acceptor ($d_e < d_i$) and another is donor ($d_e > d_i$), it is observed as complementary regions in the fingerprint graph. The two sharp spikes in the third column of Table 7 indicate this, and show the typical O-H \cdots O interaction. The contribution of this interaction to the total surface is over 25% for PQ11, PQ14, ABQ10 and ABQ17 molecules. H-H interactions are given in the second column of Table 7 and when their percentage ratios are considered, it is seen that they are the most dominant interactions. 2D fingerprint graphs for C-H /H-C interactions are in the fourth column. When the graphs are examined carefully, some of them have distinct “wings” and this corresponds to the C-H \cdots π interactions (Spackman & Byrom, 1997) (McKinnon et al., 1998). In these wings, $d_e > d_i$ states correspond to the surface points around the C-H donor, while $d_e < d_i$ states correspond to the surface points around the π acceptor (Seth et al., 2011). The partial contribution of C-H \cdots C interactions of the molecules were predicted as 11.6 %-18.4%.

The Molecular Electrostatic Potential (MESP) map is another important tool in studying intermolecular interactions in a molecular system and identifying nucleophilic and electrophilic attack localizations. These maps characterize the extremely negative to the extremely positive regions of the studied structure with colors starting from red to dark blue. Therefore, yellow color corresponds to a less negative region, while light blue indicates less positive region. The green color can be considered approximately as the neutral zone. The MESP surfaces of investigated molecules are represented in Table 6 to consider with

the Hirshfeld surfaces. The prominent colors on the maps are located around Oxygen atoms in the form of yellow-orange. This region, which indicates O-H \cdots O interactions, is considered electronegative in accordance with the Hirshfeld surface. On the other hand, the absence of dark blue color on the maps means that there are no overly positive regions.

3.5 Frontier Molecular Orbital (FMO) and Mulliken Charge Analysis

FMO energy analyzes are frequently used to determine the activities of molecular systems in many different areas, including complex or very large molecular systems. The most important orbitals in a molecule are the frontier molecular orbitals, called highest occupied molecular orbital (HOMO) and lowest unoccupied molecular orbital (LUMO), which determine the way the molecule interacts with other species. From these orbitals, HOMO characterizes electron donating ability, LUMO electron accepting ability, and the energy gap ($\Delta E = E_{LUMO} - E_{HOMO}$) between both characterizes molecular chemical stability. The energy gap is a critical parameter in determining electrical transport properties because it is largely responsible for the chemical and spectroscopic properties of molecules, as well as an indicator of electron conductivity (Atkins, 2001). As can be seen from Table 5, the first four ligands with the highest Docking Score among the studied molecules are ABQ16, AQ2, AQ6 and ABQ11. Therefore, HOMO and LUMO orbitals obtained with B3LYP/6-31G(d,p) level of theory for these ligands are shown in Fig. 11 together with their energy values and inter-orbital energy gaps. Once the HOMO and LUMO energy values of a molecule or molecular system are obtained, these values can be used to compute the other important parameters such as ionization potential, electron affinity, chemical hardness and softness, electronegativity, electronic chemical potential and electrophilic index which is expressed as the tendency of a molecule as a whole to accommodate electrons (Consonni & Todeschini, 2009). The formulas used in the calculation of the mentioned parameters and the results for each examined molecule, are listed in Table 8. A quick look at results, it can be seen that the frontier molecular energy levels of the examined structures, the energy differences between these levels and other

calculated parameters are very close to each other. When ABQ16 and ABQ11 and AQ2 and AQ6 are compared among themselves, it is seen that the results are much closer. For example, when looking at the results calculated for the *electrophilicity index*, larger values were obtained for ABQ compounds than for AQ compounds. This can be explained as, since these molecules have electronegative atoms, they increase their ability to accommodate electrons. While a similar effect is observed for *chemical softness*, the opposite is true for *chemical hardness* as expected. In addition, when the calculated energy values and the obtained molecular orbitals are evaluated together, it can be seen that the dominant electron transfer of these structures can be assigned as $\pi \rightarrow \pi^*$.

Mulliken Population Analysis is frequently used in theoretical calculations for the qualitative estimation of the partial atomic charges of a molecule. Mulliken charge affects many features of a molecular system such as dipole moment, polarizability, electronic structure etc. It quantifies how the electronic structure changes under atomic displacement, therefore, it is directly related to chemical bonds.

The net atomic charges of ABQ16, AQ2, AQ6 and ABQ11 molecules obtained by Mulliken population analysis are tabulated in Table 9. In Table 10, atomic Mulliken charges with the color index of each molecule are given and plotted. The atomic numbering in Table 9 was assigned according to the numbering given here. Based on the data in Table 9, it can be seen that the negative charge on the studied molecules is delocalized on the Oxygen atoms which bound to the ring with a double bond and on the bridging Nitrogen atom. Nitrogen atoms have a partial charge more than Oxygen atoms. While the Chlorine atoms in ABQ16 and ABQ11 molecules have a positive charge, the Mulliken charge of the Fluorine atoms in the AQ2 molecule is calculated as negative. All Hydrogen atoms have a positive charge while Carbon atoms have both negative and positive charge distribution.

4. Conclusion

In this study, a set of 39 ligands that activity values were determined experimentally and reported in the literature from the quinone family, which are known to be important structures in new drug design, were discussed. Since the training set had to be determined

appropriately for the pharmacophore modeling, 27 ligands were selected as training set and 12 ligands were selected as test set randomly. The 3D-QSAR study was performed using a field-based method and Partial Least Square (PLS) regression analysis, and the regression correlation coefficient (R^2) was obtained as approximately 0.97, and, it is understood that the estimated activity values are in good agreement with the experimental data. The generated receptor-guided alignment 3D-QSAR model has sufficient statistical significance and acceptable prediction power. When pharmacophore modeling was done, AHHR_3, which had three pharmacophore features, two hydrophobic (H), a hydrogen bond acceptor (A) and an aromatic ring (R), was determined as the model with the best scores. The enrichment report for the pharmacophore model of AHHR_3 was generated and the mapping of all chemical properties of differential pattern on active and inactive compounds was plotted. From the enrichment report, the EF, BEDROC, ROC and AUAC values are 60.3, 0.69, 0.6 and 0.76, respectively. Molecular docking study was carried out to determine the interactions between the ligands of interest and the IIEP protein. In the preparation of ligand and protein for this study, it was seen that all five sites should be considered for analysis since the SiteScore of each site more than 1 or very close to 1. After docking operation, RMSD values were obtained as 0.3669 Å and 0.5535 Å for sites 1 and 2. Considering that the upper limit of the RMSD values is generally determined as 2 Å, it is seen that there is an extremely good agreement. By investigating the interactions of each ligand and IIEP protein, ABQ16 ranked first with a DockScore of -9.55, followed by AQ2, AQ6 and ABQ11 with scores of -8.56, -8.2 and -7.64, respectively. The interaction between IIEP protein and ABQ16 ligand was carried out in detail, and found that the residue of TYR253 is very important which has a pi-pi interaction with the aromatic ring of ligand. The electrical properties of the molecules which have high DScore were determined using the DFT (B3LYP) method. Studies for each of the four molecules show that there is no significant difference in the HOMO and LUMO energy values and the energy band differences between these orbitals. In addition, with the help of Hirshfeld surface analysis, the charge distributions of the molecules were examined and evaluated, and

element-based electronic bond interactions were examined with the 2D fingerprint plot.

References

- ACUÑA, J., PIERMATTEY, J., CARO, D., BANNWITZ, S., BARRIOS, L., LÓPEZ, J., OCAMPO, Y., VIVAS-REYES, R., ARISTIZÁBAL, F., GAITÁN, R., MÜLLER, K., & FRANCO, L. (2018). Synthesis, Anti-Proliferative Activity Evaluation and 3D-QSAR Study of Naphthoquinone Derivatives as Potential Anti-Colorectal Cancer Agents. *Molecules* 2018, Vol. 23, Page 186, 23(1), 186. <https://doi.org/10.3390/MOLECULES23010186>
- ATKINS, P. W. (2001). *Physical Chemistry. The Extent of Adsorption*. Oxford University Press.
- BANERJEE, S., AZMI, A. S., PADHYE, S., SINGH, M. W., BARUAH, J. B., PHILIP, P. A., SARKAR, F. H., & MOHAMMAD, R. M. (2010). Structure-activity studies on therapeutic potential of thymoquinone analogs in pancreatic cancer. *Pharmaceutical Research*, 27(6), 1146–1158. <https://doi.org/10.1007/S11095-010-0145-3/FIGURES/8>
- BASSYOUNI, F. (2017). *Molecular Modeling and Biological Activities of New Potent Antimicrobial, Anti-Inflammatory and Anti-Nociceptive of 5-Nitro Indoline-2-One Derivatives*. <https://doi.org/10.4172/2169-0138.1000148>
- BAYRAK, N., YILDIRIM, H., YILDIZ, M., RADWAN, M. O., OTSUKA, M., FUJITA, M., CIFTCI, H. I., & TUYUN, A. F. (2020). A novel series of chlorinated plastoquinone analogs: Design, synthesis, and evaluation of anticancer activity. *Chemical Biology & Drug Design*, 95(3), 343–354. <https://doi.org/10.1111/CBDD.13651>
- BAYRAK, N., YILDIRIM, H., YILDIZ, M., RADWAN, M. O., OTSUKA, M., FUJITA, M., TUYUN, A. F., & CIFTCI, H. I. (2019). Design, synthesis, and biological activity of Plastoquinone analogs as a new class of anticancer agents. *Bioorganic Chemistry*, 92, 103255. <https://doi.org/10.1016/J.BIOORG.2019.103255>
- BECKE, A. D. (1988). Density-functional exchange-energy approximation with correct asymptotic behavior. *Physical Review A*, 38(6), 3098. <https://doi.org/10.1103/PhysRevA.38.3098>
- BELORGEY, D., ANTOINE LANFRANCHI, D., & DAVIOUD-CHARVET, E. (2013). 1,4-Naphthoquinones and Other NADPH-Dependent Glutathione Reductase-Catalyzed Redox Cyclers as Antimalarial Agents. *Current Pharmaceutical Design*, 19(14), 2512–2528.
- BERMAN, H. M., WESTBROOK, J., FENG, Z., GILLILAND, G., BHAT, T. N., WEISSIG, H., SHINDYALOV, I. N., & BOURNE, P. E. (2000). The Protein Data Bank. *Nucleic Acids Research*, 28(1), 235–242. <https://doi.org/10.1093/NAR/28.1.235>
- BERNSTEIN, F. C., KOETZLE, T. F., WILLIAMS, G. J. B., MEYER, E. F., BRICE, M. D., RODGERS, J. R., KENNARD, O., SHIMANOUCI, T., & TASUMI, M. (1977). The protein data bank: A computer-based archival file for macromolecular structures. *Journal of Molecular Biology*, 112(3), 535–542. [https://doi.org/10.1016/S0022-2836\(77\)80200-3](https://doi.org/10.1016/S0022-2836(77)80200-3)
- BRANDY, Y., ONONIWU, I., ADEDEJI, D., WILLIAMS, V., MOUAMBA, C., KANAAN, Y., COPELAND, R. L., WRIGHT, D. A., BUTCHER, R. J., DENMEADE, S. R., & BAKARE, O. (2012). Synthesis and cytotoxic activities of some 2-Arylnaphtho [2,3-d]oxazole-4,9-dione derivatives on androgen-dependent (LNCaP) and androgen-independent (PC3) human prostate cancer cell lines. *Investigational New Drugs*, 30(4), 1709–1714. <https://doi.org/10.1007/S10637-011-9635-3/TABLES/2>
- BRANNON-PEPPAS, L., & BLANCHETTE, J. O. (2004). Nanoparticle and targeted systems for cancer therapy. *Advanced Drug Delivery Reviews*, 56(11), 1649–1659. <https://doi.org/10.1016/J.ADDR.2004.02.014>
- CIFTCI, H. I., BAYRAK, N., YILDIRIM, H., YILDIZ, M., RADWAN, M. O., OTSUKA, M., FUJITA, M., & TUYUN, A. F. (2019). Discovery and structure–activity relationship of plastoquinone analogs as anticancer agents against chronic myelogenous leukemia cells. *Archiv Der Pharmazie*, 352(12), 1900170. <https://doi.org/10.1002/ARDP.201900170>
- CONSONNI, V., & TODESCHINI, R. (2009). *Molecular Descriptors for Chemoinformatics: Volume I: Alphabetical Listing/Volume II: Appendices, References*. John Wiley & Sons,

- Ltd.
- DEY, D., RAY, R., & HAZRA, B. (2014). Antitubercular and Antibacterial Activity of Quinonoid Natural Products Against Multi-Drug Resistant Clinical Isolates. *Phytotherapy Research*, 28(7), 1014–1021. <https://doi.org/10.1002/PTR.5090>
- DU, X., LI, Y., XIA, Y. L., AI, S. M., LIANG, J., SANG, P., JI, X. L., & LIU, S. Q. (2016). Insights into Protein–Ligand Interactions: Mechanisms, Models, and Methods. *International Journal of Molecular Sciences* 2016, Vol. 17, Page 144, 17(2), 144. <https://doi.org/10.3390/IJMS17020144>
- EVANS, D. A., DOMAN, T. N., THORNER, D. A., & BODKIN, M. J. (2007). 3D QSAR methods: Phase and catalyst compared. *Journal of Chemical Information and Modeling*, 47(3), 1248–1257. <https://doi.org/10.1021/CI7000082/ASSET/IMAGES/MEDIUM/CI7000082N00001.GIF>
- FRISCH, M. J., TRUCKS, G. W., SCHLEGEL, H. B., SCUSERIA, G. E., ROBB, M. A., CHEESEMAN, J. R., SCALMANI, G., BARONE, V., PETERSSON, G. A., NAKATSUJI, H., LI, X., CARICATO, M., MARENICH, A., BLOINO, J., JANESKO, B. G., GOMPERS, R., MENNUCCI, B., HRATCHIAN, H. P., ORTIZ, J. V., ... FOX, D. J. (2016). *Gaussian 09* (Revision A.02). Gaussian, Inc.
- GLAMOČLIJA, U., PADHYE, S., ŠPIRTOVIĆ-HALILOVIĆ, S., OSMANOVIĆ, A., VELJOVIĆ, E., ROCA, S., NOVAKOVIĆ, I., MANDIĆ, B., TUREL, I., KLJUN, J., TRIFUNOVIĆ, S., KAHROVIĆ, E., PAVELIĆ, S. K., HAREJ, A., KLOBUČAR, M., & ZAVRŠNIK, D. (2018). Synthesis, Biological Evaluation and Docking Studies of Benzoxazoles Derived from Thymoquinone. *Molecules* 2018, Vol. 23, Page 3297, 23(12), 3297. <https://doi.org/10.3390/MOLECULES23123297>
- GODOY-CASTILLO, C., BRAVO-ACUÑA, N., ARRIAGADA, G., FAUNES, F., LEÓN, R., & SOTO-DELGADO, J. (2021). Identification of the naphthoquinone derivative inhibitors binding site in heat shock protein 90: an induced-fit docking, molecular dynamics and 3D-QSAR study. *Journal of Biomolecular Structure and Dynamics*, 39(16), 5977–5987. https://doi.org/10.1080/07391102.2020.1803134/SUPPL_FILE/TBSD_A_1803134_SM9783.PDF
- GOTTESMAN, M. M. (2001). *MECHANISMS OF CANCER DRUG RESISTANCE*.
- GREENWOOD, J. R., CALKINS, D., SULLIVAN, A. P., & SHELLEY, J. C. (2010). Towards the comprehensive, rapid, and accurate prediction of the favorable tautomeric states of drug-like molecules in aqueous solution. *Journal of Computer-Aided Molecular Design*, 24(6–7), 591–604. <https://doi.org/10.1007/S10822-010-9349-1/FIGURES/6>
- HALGREN, T. (2007). New Method for Fast and Accurate Binding-site Identification and Analysis. *Chemical Biology & Drug Design*, 69(2), 146–148. <https://doi.org/10.1111/J.1747-0285.2007.00483.X>
- HALGREN, T. A. (2009). Identifying and characterizing binding sites and assessing druggability. *Journal of Chemical Information and Modeling*, 49(2), 377–389. https://doi.org/10.1021/CI800324M/ASSET/IMAGES/MEDIUM/CI-2008-00324M_0006.GIF
- HARDER, E., DAMM, W., MAPLE, J., WU, C., REBOUL, M., XIANG, J. Y., WANG, L., LUPYAN, D., DAHLGREN, M. K., KNIGHT, J. L., KAUS, J. W., CERUTTI, D. S., KRILOV, G., JORGENSEN, W. L., ABEL, R., & FRIESNER, R. A. (2016). OPLS3: A Force Field Providing Broad Coverage of Drug-like Small Molecules and Proteins. *Journal of Chemical Theory and Computation*, 12(1), 281–296. https://doi.org/10.1021/ACS.JCTC.5B00864/SUPPL_FILE/CT5B00864_SI_001.ZIP
- HIRSHFELD, F. L. (1977). Bonded-atom fragments for describing molecular charge densities. *Theoretica Chimica Acta* 1977 44:2, 44(2), 129–138. <https://doi.org/10.1007/BF00549096>
- JANECZKO, M., DEMCHUK, O. M., STRZELECKA, D., KUBIŃSKI, K., & MASŁYK, M. (2016). New family of antimicrobial agents derived from 1,4-naphthoquinone. *European Journal of Medicinal Chemistry*, 124, 1019–1025. <https://doi.org/10.1016/J.EJMECH.2016.10.034>
- JOHNSON-AJINWO, O. R., ULLAH, I., MBYE, H., RICHARDSON, A., HORROCKS, P., & LI, W. W. (2018). The synthesis and evaluation of

- thymoquinone analogues as anti-ovarian cancer and antimalarial agents. *Bioorganic & Medicinal Chemistry Letters*, 28(7), 1219–1222.
<https://doi.org/10.1016/J.BMCL.2018.02.051>
- JORDÃO, A. K., NOVAIS, J., LEAL, B., ESCOBAR, A. C., DOS SANTOS JÚNIOR, H. M., CASTRO, H. C., & FERREIRA, V. F. (2013). Synthesis using microwave irradiation and antibacterial evaluation of new N,O-acetals and N,S-acetals derived from 2-amino-1,4-naphthoquinones. *European Journal of Medicinal Chemistry*, 63, 196–201.
<https://doi.org/10.1016/J.EJMECH.2013.01.010>
- KADELA-TOMANEK, M., JASTRZĘBSKA, M., PAWEŁCZAK, B., BĘBENEK, E., CHROBAK, E., LATOCHA, M., KSIĄŻEK, M., KUSZ, J., & BORYCZKA, S. (2017). Alkynyloxy derivatives of 5,8-quinolinedione: Synthesis, in vitro cytotoxicity studies and computational molecular modeling with NAD(P)H:Quinone oxidoreductase 1. *European Journal of Medicinal Chemistry*, 126, 969–982.
<https://doi.org/10.1016/J.EJMECH.2016.12.031>
- KUNNUMAKKARA, A. B., BORDOLOI, D., SAILO, B. L., ROY, N. K., THAKUR, K. K., BANIK, K., SHAKIBAEI, M., GUPTA, S. C., & AGGARWAL, B. B. (2019). Cancer drug development: The missing links. *Experimental Biology and Medicine*, 244(8), 663–689.
https://doi.org/10.1177/1535370219839163/ASSET/IMAGES/LARGE/10.1177_1535370219839163-FIG2.JPEG
- LEE, C., YANG, W., & PARR, R. G. (1988). Development of the Colle-Salvetti correlation-energy formula into a functional of the electron density. *Physical Review B*, 37(2), 785.
<https://doi.org/10.1103/PhysRevB.37.785>
- LÓPEZ-LIRA, C., ALZATE-MORALES, J. H., PAULINO, M., MELLA-RAIPÁN, J., SALAS, C. O., TAPIA, R. A., & SOTO-DELGADO, J. (2018). Combined molecular modelling and 3D-QSAR study for understanding the inhibition of NQO1 by heterocyclic quinone derivatives. *Chemical Biology & Drug Design*, 91(1), 29–38.
<https://doi.org/10.1111/CBDD.13051>
- MADHAVI SASTRY, G., ADZHIGIREY, M., DAY, T., ANNABHIMOJU, R., & SHERMAN, W. (2013). Protein and ligand preparation: Parameters, protocols, and influence on virtual screening enrichments. *Journal of Computer Aided Molecular Design*, 27(3), 221–234.
<https://doi.org/10.1007/S10822-013-9644-8/TABLES/9>
- MCKINNON, J. J., MITCHELL, A. S., & SPACKMAN, M. A. (1998). Hirshfeld surfaces: a new tool for visualising and exploring molecular crystals. *Chemistry—A European Journal*, 4(11), 2136–2141.
- MILLER, M. D., SHERIDAN, R. P., & KEARSLEY, S. K. (1999). SQ: A program for rapidly producing pharmacophorically relevant molecular superpositions. *Journal of Medicinal Chemistry*, 42(9), 1505–1514.
https://doi.org/10.1021/JM9806143/SUPPL_FILE/JM9806143_S.PDF
- NAGAR, B., BORNMANN, W. G., PELLICENA, P., SCHINDLER, T., VEACH, D. R., MILLER, W. T., CLARKSON, B., & KURIYAN, J. (2002). Crystal Structures of the Kinase Domain of c-Abl in Complex with the Small Molecule Inhibitors PD173955 and Imatinib (STI-571). *Biochemistry and Biophysics*, 62(15), 4236–4243.
- OLGEN, S. (2018). Overview on Anticancer Drug Design and Development. *Current Medicinal Chemistry*, 25(15), 1704–1719.
<https://doi.org/10.2174/0929867325666171129215610>
- RAVICHANDIRAN, P., PREMNATH, D., & VASANTHKUMAR, S. (2014). Synthesis, molecular docking and antibacterial evaluation of new 1,4-naphthoquinone derivatives contains carbazole-6,11-dione moiety. *Journal of Chemical Biology* 2014 7:3, 7(3), 93–101.
<https://doi.org/10.1007/S12154-014-0115-Z>
- RYU, C. K., OH, S. Y., CHOI, S. J., & KANG, D. Y. (2014). Synthesis of Antifungal Evaluation of 2H-[1,2,3]Triazol[4,5-g]isoquinoline-4,9-diones. *Chemical and Pharmaceutical Bulletin*, 62(11), c14-00527.
<https://doi.org/10.1248/CPB.C14-00527>
- SCHRÖDINGER RELEASE: PHASE (NO. 4). (2020). Schrödinger, LLC.
- SCHRÖDINGER RELEASE: EPIK (NO. 4). (2020). Schrödinger, LLC.
- SCHRÖDINGER RELEASE: GLIDE, (NO. 4). (2020). Schrödinger, LLC.
- SCHRÖDINGER RELEASE: LIGPREP (NO. 4). (2020). Schrödinger, LLC.

- SCHRÖDINGER RELEASE: SITEMAP (NO. 4). (2020). Schrödinger, LLC.
- SCHRÖDINGER RELEASE (NO. 4). (2020). Maestro, Schrödinger, LLC.
- SENDL, A., CHEN, J. L., JOLAD, S. D., STODDART, C., ROZHON, E., KERNAN, M., NANAKORN, W., & BALICK, M. (1996). Two New Naphthoquinones with Antiviral Activity from *Rhinacanthus nasutus*. *Journal of Natural Products*, 59(8), 808–811. <https://doi.org/10.1021/NP9601871>
- SETH, S. K., MAITY, G. C., & KAR, T. (2011). Structural elucidation, Hirshfeld surface analysis and quantum mechanical study of par-nitro benzylidene methyl arjunolate. *Journal of Molecular Structure*, 1000(1–3), 120–126. <https://doi.org/10.1016/J.MOLSTRUC.2011.06.003>
- SHELLEY, J. C., CHOLLETI, A., FRYE, L. L., GREENWOOD, J. R., TIMLIN, M. R., & UCHIMAYA, M. (2007). Epik: A software program for pKa prediction and protonation state generation for drug-like molecules. *Journal of Computer-Aided Molecular Design*, 21(12), 681–691. <https://doi.org/10.1007/S10822-007-9133-Z/TABLES/5>
- SHI, J., LONG, T., ZHOU, Y., WANG, L., JIANG, C., PAN, D., & ZHU, X. (2021). Efficiency and Quantitative Structure-Activity Relationship of Monoaromatics Oxidation by Quinone-Activated Persulfate. *Frontiers in Chemistry*, 9, 172. <https://doi.org/10.3389/FCHEM.2021.580643/XML/NLM>
- SIEGEL, R. L., MILLER, K. D., & JEMAL, A. (2016). CANCER STATISTICS, 2016. *CA: A Cancer Journal for Clinicians*, 66(1), 7–30. <https://doi.org/10.3322/CAAC.21332>
- SOUSA, S. F., RIBEIRO, A. J. M., COIMBRA, J. T. S., NEVES, R. P. P., MARTINS, S. A., MOORTHY, N. S. H. N., FERNANDES, P. A., & RAMOS, M. J. (2013). Protein-Ligand Docking in the New Millennium – A Retrospective of 10 Years in the Field. *Current Medicinal Chemistry*, 20(18), 2296–2314.
- SPACKMAN, M. A., & BYROM, P. G. (1997). A novel definition of a molecule in a crystal. *Chemical Physics Letters*, 267(3–4), 215–220. [https://doi.org/10.1016/S0009-2614\(97\)00100-0](https://doi.org/10.1016/S0009-2614(97)00100-0)
- SPACKMAN, M. A., & JAYATILAKA, D. (2009). Hirshfeld surface analysis. *CrystEngComm*, 11(1), 19–32. <https://doi.org/10.1039/B818330A>
- SPACKMAN, M. A., & MCKINNON, J. J. (2002). Fingerprinting intermolecular interactions in molecular crystals. *CrystEngComm*, 4(66), 378–392.
- TROPSHA, A. (2010). Best Practices for QSAR Model Development, Validation, and Exploitation. *Molecular Informatics*, 29(6–7), 476–488. <https://doi.org/10.1002/MINF.201000061>
- TURNER, M., KINNON, J. M., S. WOLFF, GRIMWOOD, D., SPACKMAN, P., JAYATILAKA, D., & SPACKMAN, M. (2017). *CrystalExplorer17*. University of Western Australia.
- VIDLER, L. R., BROWN, N., KNAPP, S., & HOELDER, S. (2012). Druggability analysis and structural classification of bromodomain acetyl-lysine binding sites. *Journal of Medicinal Chemistry*, 55(17), 7346–7359. https://doi.org/10.1021/JM300346W/SUPPL_FILE/JM300346W_SI_002.PDF
- WELLINGTON, K. W. (2015). *Understanding cancer and the anticancer activities of naphthoquinones-a review*. <https://doi.org/10.1039/c4ra13547d>
- WELLINGTON, K. W., KOLESNIKOVA, N. I., NYOKA, N. B. P., & MCGAW, L. J. (2019). Investigation of the antimicrobial and anticancer activity of aminonaphthoquinones. *Drug Development Research*, 80(1), 138–146. <https://doi.org/10.1002/DDR.21477>

Table 6. The Hirshfeld and Molecular Electronic Potential (MEP) Surfaces for the ligands that experimentally crystallographic structures are available

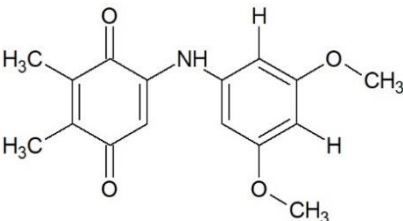
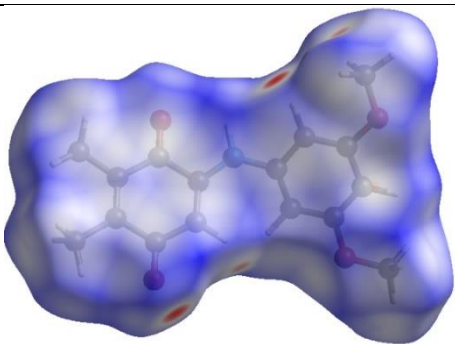
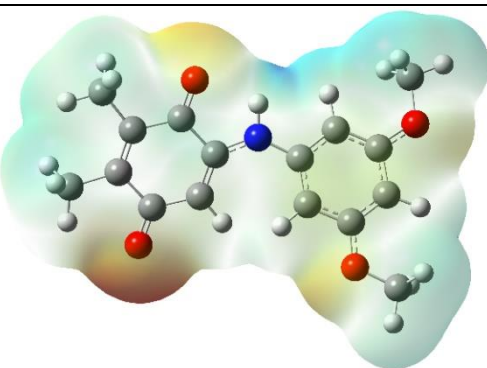
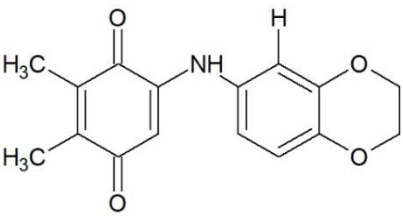
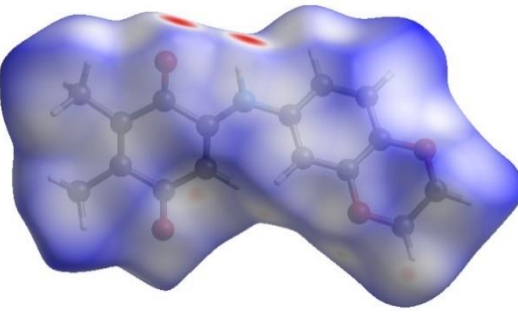
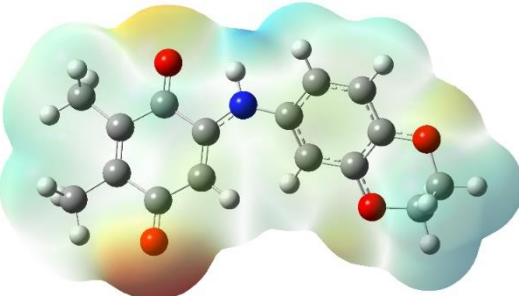
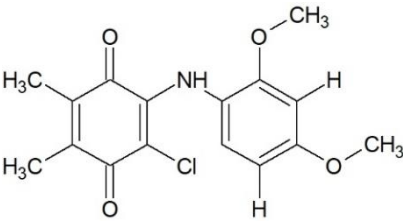
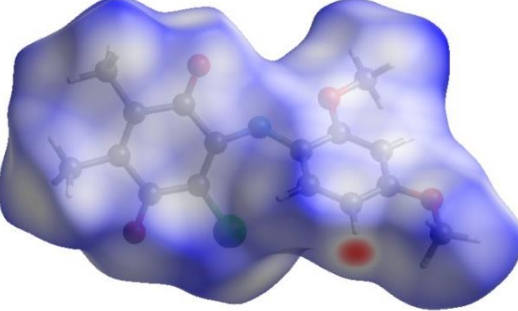
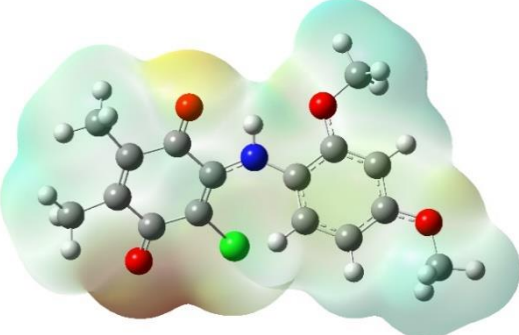
Ligand Name	Ligand Structure	Hirshfeld Surface (d_{norm})	Molecular Electrostatic Potential (MESP) Surface
PQ11		 -0.1986 (red color) 1.1136 (blue color)	
PQ14		 -0.2896 (red color) 1.3363 (blue color)	
ABQ10		 -0.2598 (red color) 1.2592 (blue color)	

Table 6. Continued

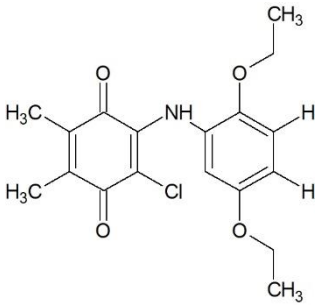
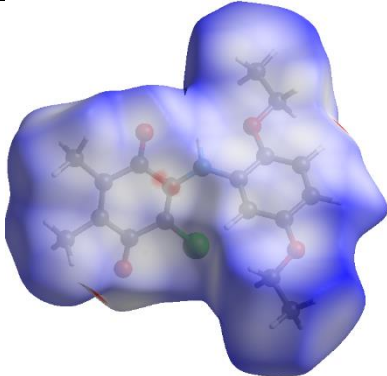
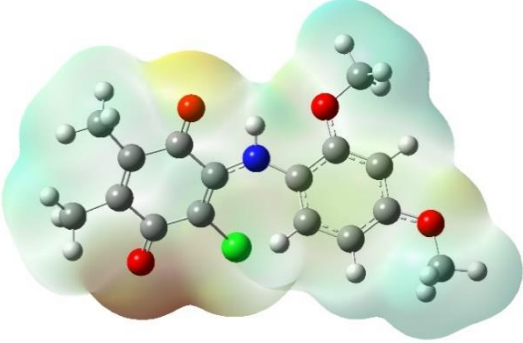
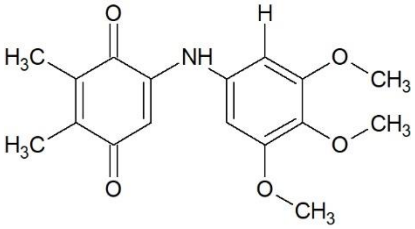
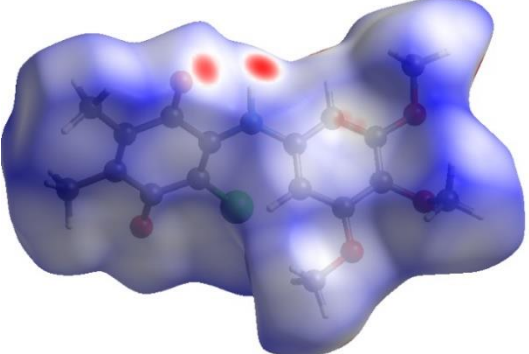
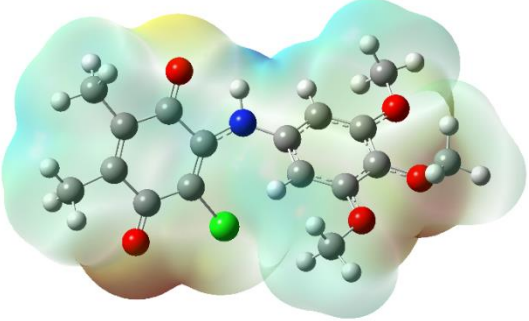
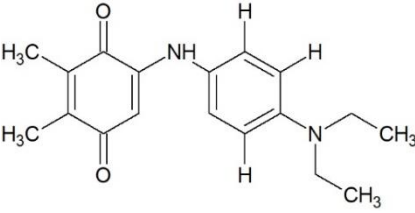
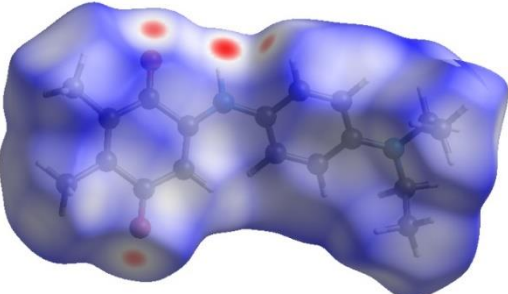
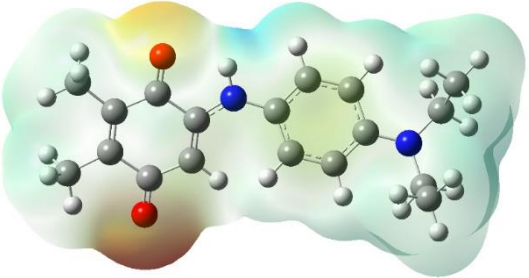
Ligand Name	Ligand Structure	Hirshfeld Surface (d_{norm})	Molecular Electrostatic Potential (MESP) Surface
ABQ14		 -0.1566 (red color) 1.6257 (blue color)	
ABQ17		 -0.2367 (red color) 1.4253 (blue color)	
AQ9		 -0.2051 (red color) 1.3109 (blue color)	

Table 6. Continued

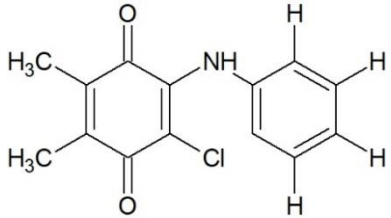
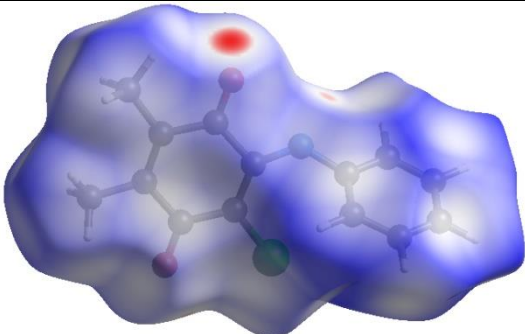
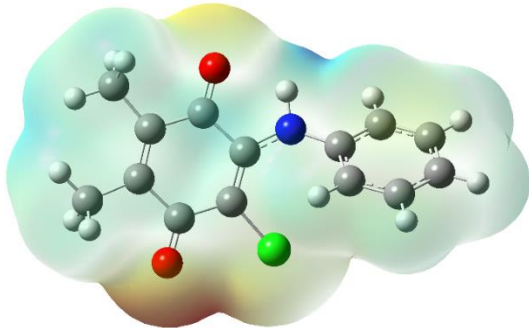
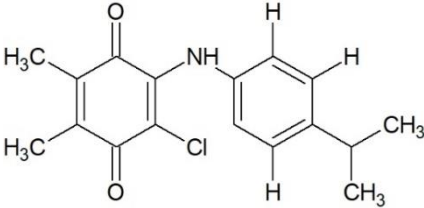
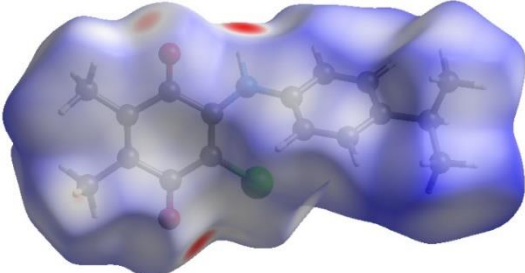
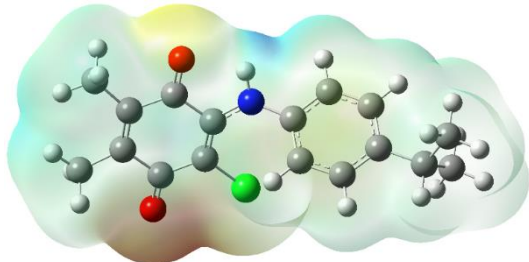
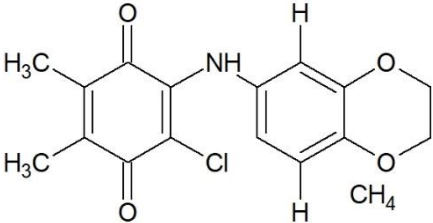
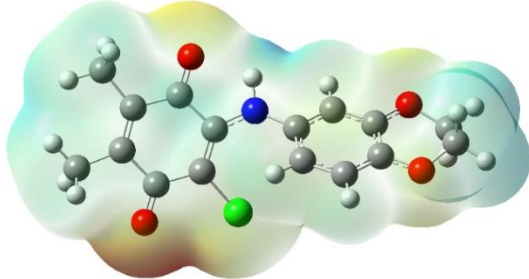
Ligand Name	Ligand Structure	Hirshfeld Surface (d_{norm})	Molecular Electrostatic Potential (MESP) Surface
AQ11		 -0.1445 (red color) 1.1977 (blue color)	
AQ17		 -0.3922 (red color) 1.5692 (blue color)	
ABQ16		*.cif file of molecule is not available	

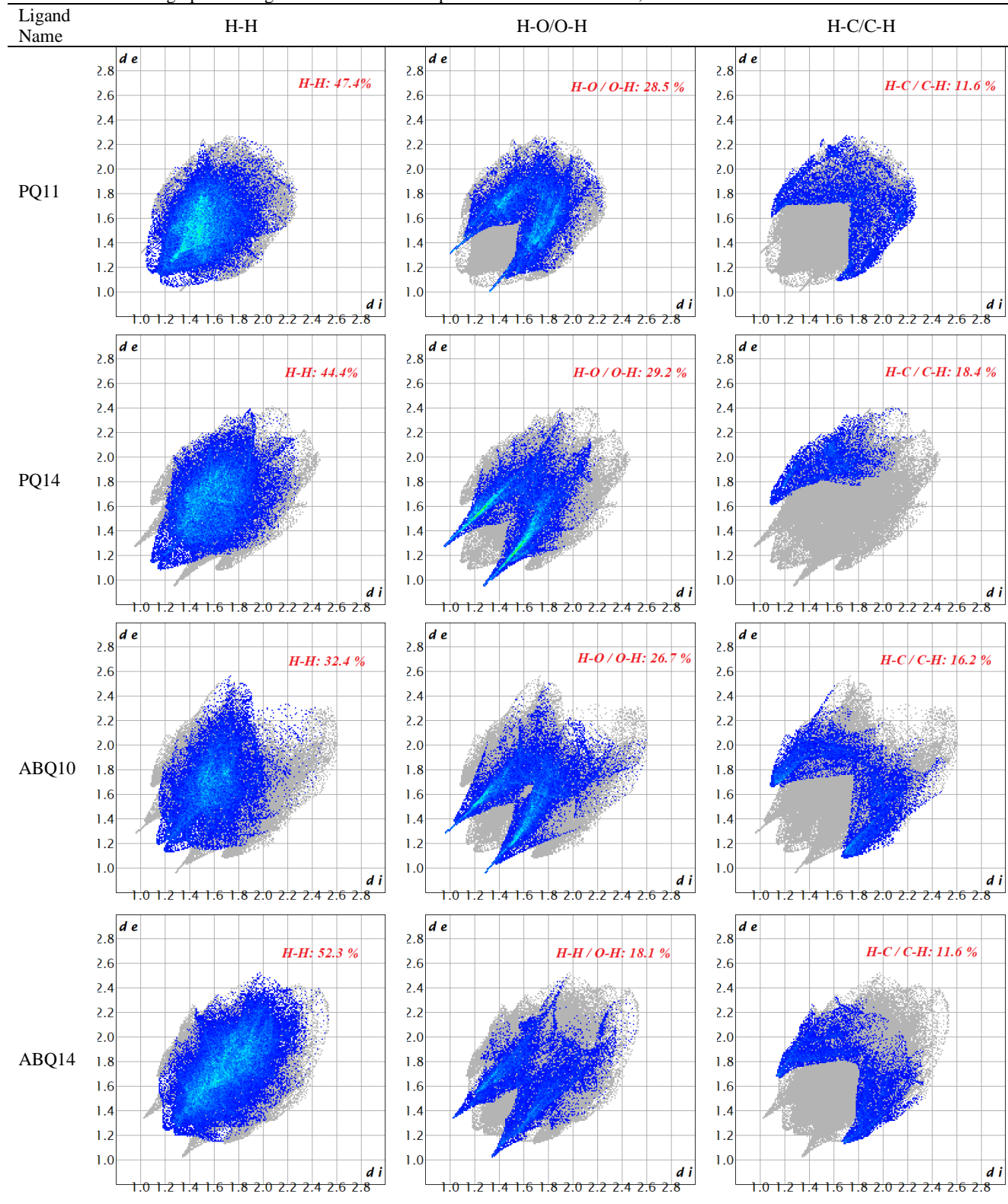
Table 7. The 2D fingerprint histogram of the related compounds resolved into O...H, C...H and H...H contacts

Table 7. Continued

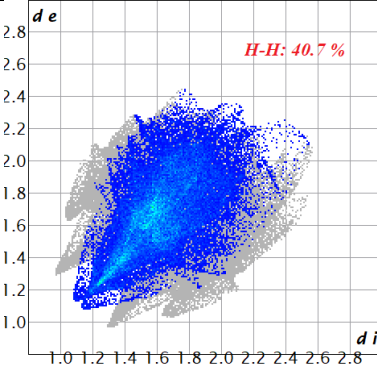
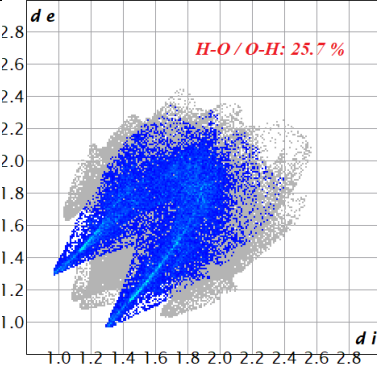
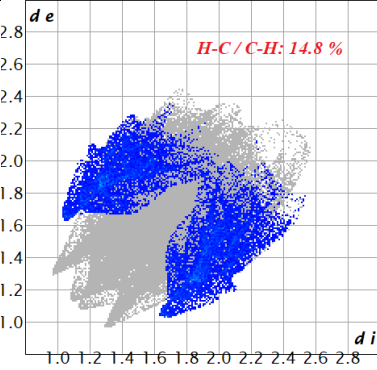
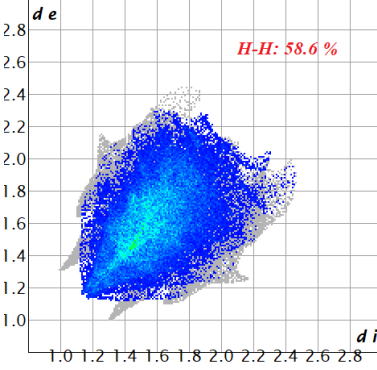
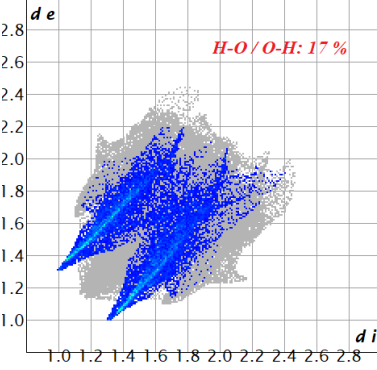
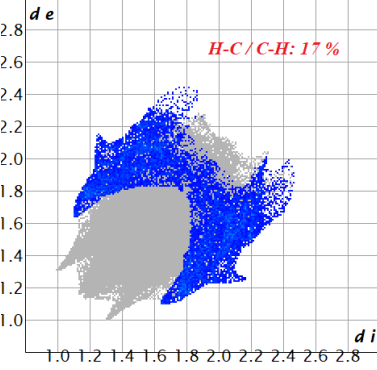
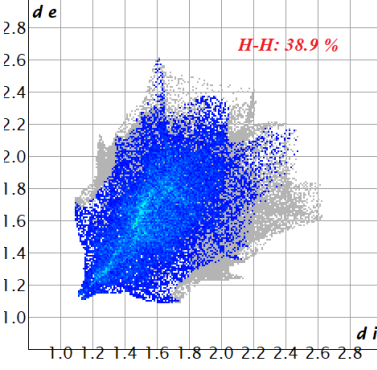
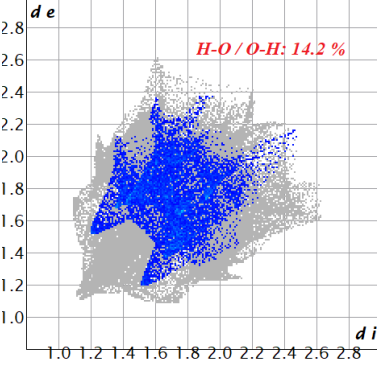
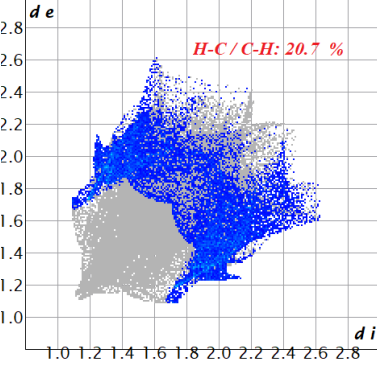
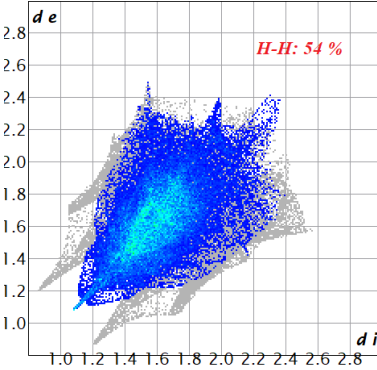
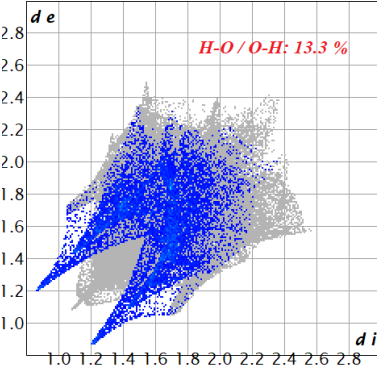
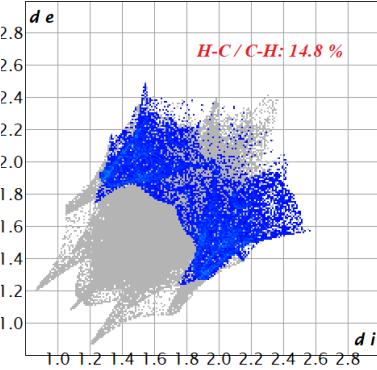
Ligand Name	H-H	H-O/O-H	H-C/C-H
ABQ17	 <p><i>H-H: 40.7 %</i></p>	 <p><i>H-O/O-H: 25.7 %</i></p>	 <p><i>H-C/C-H: 14.8 %</i></p>
AQ9	 <p><i>H-H: 58.6 %</i></p>	 <p><i>H-O/O-H: 17 %</i></p>	 <p><i>H-C/C-H: 17 %</i></p>
AQ11	 <p><i>H-H: 38.9 %</i></p>	 <p><i>H-O/O-H: 14.2 %</i></p>	 <p><i>H-C/C-H: 20.7 %</i></p>
AQ17	 <p><i>H-H: 54 %</i></p>	 <p><i>H-O/O-H: 13.3 %</i></p>	 <p><i>H-C/C-H: 14.8 %</i></p>

Table 8. The HOMO&LUMO energy and computed other parameters

Parameters	Formula	ABQ16	AQ2	AQ6	ABQ11
LUMO energy (eV)	E_{LUMO}	-3.038	-3.059	-2.903	-3.032
HOMO energy (eV)	E_{HOMO}	-5.475	-6.043	-5.652	-5.266
Energy band gap	$\Delta E = E_{LUMO} - E_{HOMO}$	2.437	2.984	2.749	2.234
Ionization potential	$I = -E_{HOMO}$	5.475	6.043	5.652	5.266
Electron affinity	$A = -E_{LUMO}$	3.038	3.059	2.903	3.032
Chemical hardness	$\eta = (I - A)/2$	1.219	1.492	1.375	1.117
Chemical softness	$\xi = 1/2\eta$	0.410	0.335	0.364	0.448
Electronegativity	$\chi = (I + A)/2$	4.257	4.551	4.278	4.149
Chemical potential	$\mu = -(I + A)/2$	-4.257	-4.551	-4.278	-4.149
Electrophilicity index	$\psi = \mu^2/2\eta$	7.434	6.941	6.656	7.706

Table 9. Mulliken atomic charges

ABQ16		AQ2		AQ6		ABQ11	
Atom	Charge	Atom	Charge	Atom	Charge	Atom	Charge
C (1)	0,4216	C (1)	0,3925	C (1)	0,3916	C (1)	0,4220
C (2)	-0,2350	C (2)	-0,1898	C (2)	-0,1926	C (2)	-0,2376
C (3)	0,3183	C (3)	0,3159	C (3)	0,3144	C (3)	0,3197
C (4)	0,3747	C (4)	0,3708	C (4)	0,3708	C (4)	0,3742
C (5)	0,0276	C (5)	0,0213	C (5)	0,0208	C (5)	0,0269
C (6)	0,0233	C (6)	0,0374	C (6)	0,0372	C (6)	0,0231
C (7)	-0,3588	C (8)	-0,3603	C (8)	-0,3596	C (7)	-0,3585
C (11)	-0,3607	C (12)	-0,3925	C (12)	-0,3925	C (11)	-0,3616
O (15)	-0,4911	O (16)	-0,4861	O (16)	-0,4968	O (15)	-0,4859
O (16)	-0,4669	O (17)	-0,4923	O (17)	-0,4983	O (16)	-0,4693
N (17)	-0,6775	N (18)	-0,7146	N (18)	-0,6874	N (17)	-0,6746
C (18)	-0,1435	C (19)	-0,0905	C (19)	-0,1362	C (18)	0,3432
C (19)	0,3188	C (20)	-0,0850	C (20)	0,1280	C (19)	-0,1251
C (20)	0,3200	C (21)	-0,1198	C (21)	-0,1241	C (20)	-0,1352
C (21)	-0,1669	C (22)	-0,0733	C (22)	-0,1185	C (21)	0,3282
C (22)	0,2831	C (23)	0,3125	C (23)	0,3144	C (22)	0,2590
C (23)	-0,0794	C (24)	-0,1006	C (24)	-0,0983	C (23)	-0,1355
Cl (28)	0,0246	C (30)	0,8162	C (29)	-0,3819	Cl (26)	0,0220
O (29)	-0,5322	F (31)	-0,2642	H (7)	0,1062	O (27)	-0,5427
O (30)	-0,5297	F (32)	-0,2749	H (9)	0,1363	C (28)	-0,0798
C (31)	0,0275	F (33)	-0,2601	H (10)	0,1106	O (33)	-0,5262
C (32)	0,0289	H (7)	0,1096	H (11)	0,1351	C (34)	-0,0834
H (8)	0,1393	H (9)	0,1396	H (13)	0,1272	H (8)	0,1399
H (9)	0,1112	H (10)	0,1115	H (14)	0,1275	H (9)	0,1105
H (10)	0,1368	H (11)	0,1369	H (15)	0,1538	H (10)	0,1365
H (12)	0,1078	H (13)	0,1284	H (25)	0,0862	H (12)	0,1087
H (13)	0,1457	H (14)	0,1296	H (26)	0,0844	H (13)	0,1446
H (14)	0,1457	H (15)	0,1537	H (27)	0,1060	H (14)	0,1454
H (24)	0,1046	H (25)	0,1034	H (28)	0,2844	H (24)	0,1057
H (25)	0,1038	H (26)	0,0992	H (30)	0,1291	H (25)	0,2993
H (26)	0,2918	H (27)	0,1155	H (31)	0,1165	H (29)	0,1165
H (27)	0,1030	H (28)	0,1163	H (32)	0,1154	H (30)	0,1288
H (33)	0,1190	H (29)	0,2941	H (33)	0,0903	H (31)	0,1149
H (34)	0,1212					H (32)	0,0916
H (35)	0,1244					H (35)	0,1257
H (36)	0,1188					H (36)	0,1238
						H (37)	0,1089
						H (38)	0,0962

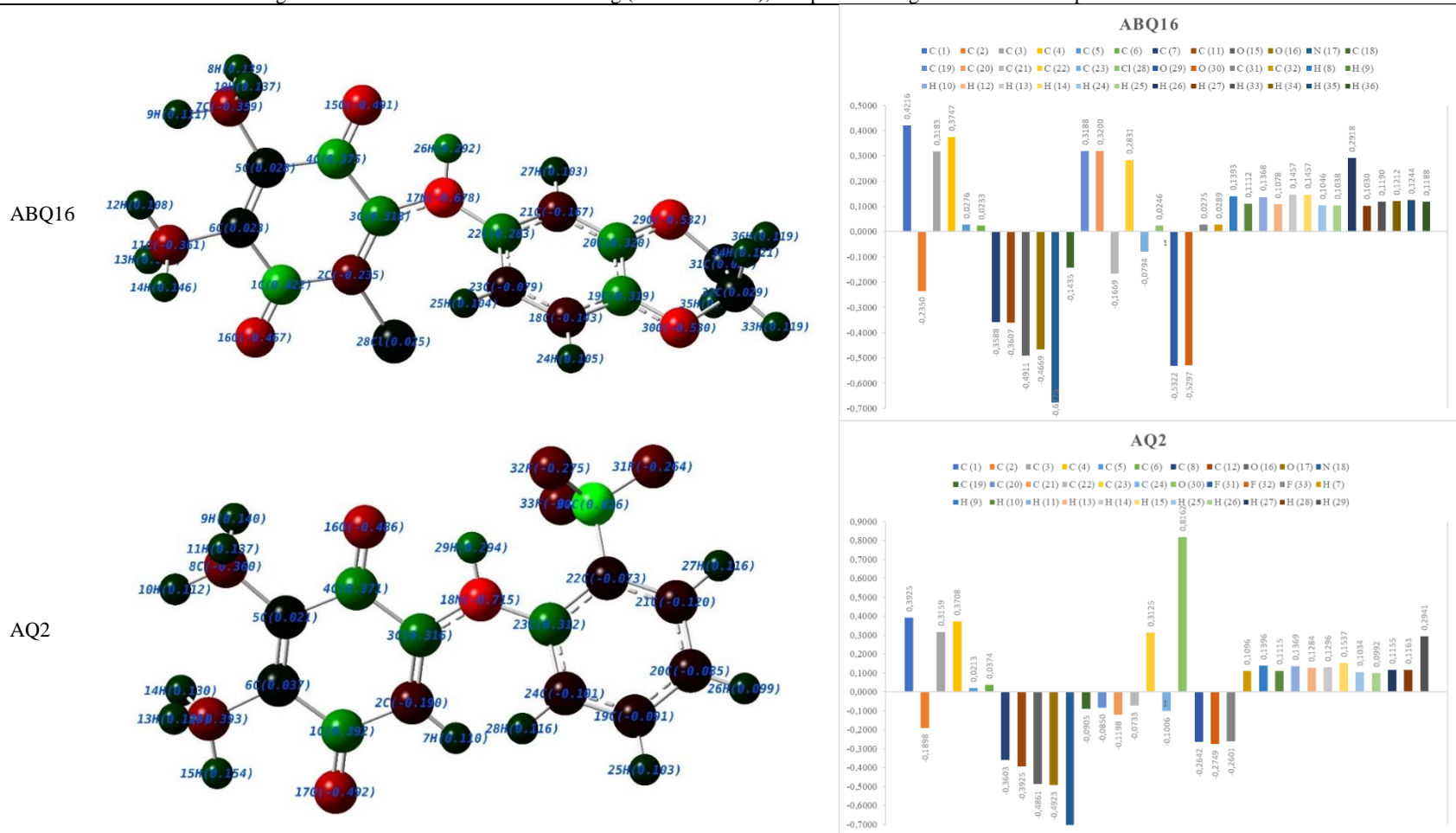
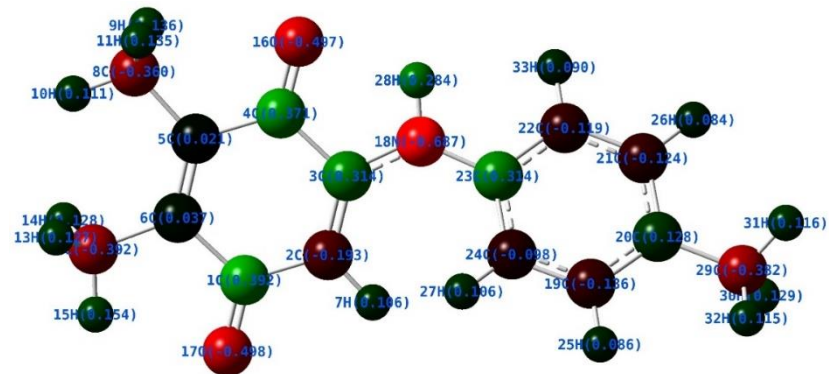
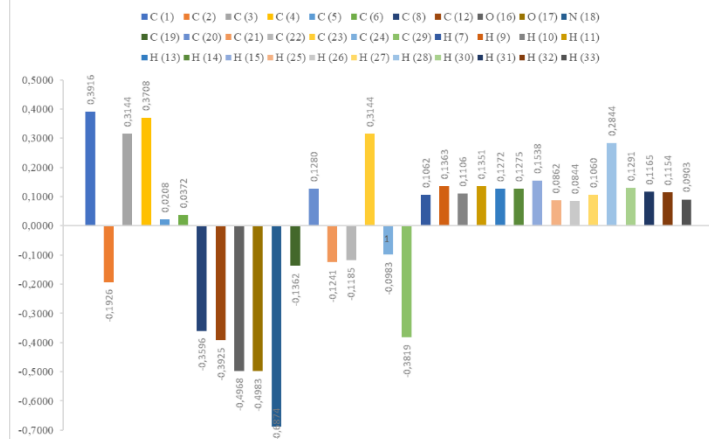
Table 10. Mulliken atomic charges with color index and atom numbering (second column), and plotted charge values of each separate atom

Table 10. Continued

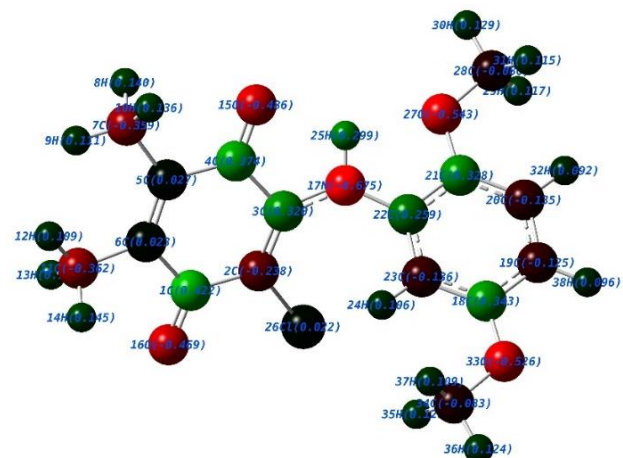
AQ6



AQ6



ABQ11



ABQ11

